Materials Today Bio 25 (2024) 100954

Contents lists available at ScienceDirect

Materials Today Bio

journal homepage: www.journals.elsevier.com/materials-today-bio

Biocompatible and bioactivable terpolymer-lipid-MnO_2 Nanoparticle-based MRI contrast agent for improving tumor detection and delineation

Tin-Yo C. Yen [a,1], Azhar Z. Abbasi [a,1], Chungsheng He [a,1], Ho-Yin Lip [a], Elliya Park [a], Mohammad A. Amini [a], Hibret A. Adissu [c], Warren Foltz [d], Andrew M. Rauth [b,e], Jeffrey Henderson [b], Xiao Yu Wu [a,*]

[a] Leslie Dan Faculty of Pharmacy, University of Toronto, Toronto, ON, Canada
[b] Departments of Medical Biophysics and Radiation Oncology, University of Toronto, Toronto, Ontario, Canada
[c] 218 Johnson Meadow St, Gaithersburg, MD, 20878, USA
[d] STTARR Innovation Centre, Department of Radiation Oncology, Princess Margaret Hospital, Toronto, Ontario, M5G 2M9, Canada
[e] Princess Margaret Cancer Center, University Health Network, Toronto, Ontario, Canada

ARTICLE INFO

Keywords:
MRI contract agent
Tumor imaging
Manganese dioxide nanoparticles
Biocompatibility
Biodistribution and kinetics

ABSTRACT

Early and precise detection of solid tumor cancers is critical for improving therapeutic outcomes. In this regard, magnetic resonance imaging (MRI) has become a useful tool for tumor diagnosis and image-guided therapy. However, its effectiveness is limited by the shortcomings of clinically available gadolinium-based contrast agents (GBCAs), i.e. poor tumor penetration and retention, and safety concerns. Thus, we have developed a novel nanoparticulate contrast agent using a biocompatible terpolymer and lipids to encapsulate manganese dioxide nanoparticles (TPL-MDNP). The TPL-MDNP accumulated in tumor tissue and produced paramagnetic Mn^{2+} ions, enhancing T_1-weight MRI contrast *via* the reaction with H_2O_2 rich in the acidic tumor microenvironment. Compared to the clinically used GBCA, Gadovist®1.0, TPL-MDNP generated stronger T_1-weighted MR signals by over 2.0-fold at 30 % less of the recommended clinical dose with well-defined tumor delineation in preclinical orthotopic tumor models of brain, breast, prostate, and pancreas. Importantly, the MRI signals were retained for 60 min by TPL-MDNP, much longer than Gadovist®1.0. Biocompatibility of TPL-MDNP was evaluated and found to be safe up to 4-fold of the dose used for MRI. A robust large-scale manufacturing process was developed with batch-to-batch consistency. A lyophilization formulation was designed to maintain the nanostructure and storage stability of the new contrast agent.

1. Introduction

Cancer remains a leading cause of death worldwide with an estimated 19.3 million new cancer cases and almost 10.0 million cancer-related deaths in 2022 [1]. It is predicted that by 2030, 30 million people will suffer and die from cancer each year [1,2]. While effective treatment and post-treatment cancer management remain crucial, early and precise tumor detection and delineation is one of the strongest drivers for improvements in cancer treatment with respect to cancer mortality rates [3–5]. Improvements in the sensitivity and accuracy of diagnostic imaging play a key role in effective cancer treatment planning and outcomes. For instance, the detection of tumors with precise margins is crucial for oncologists to apply and facilitate curative tumor resection during surgery, as well as providing targeted treatments in case of radiation therapy (RT) [6]. Therefore, precise tumor delineation using an appropriate imaging technique that is sensitive with a high signal-to-noise ratio is of utmost importance in improving cancer treatment outcomes.

Currently clinically employed imaging techniques for cancer diagnosis include magnetic resonance imaging (MRI), positron emission tomography (PET), X-ray computed tomography (CT), single photon emission CT (SPECT), and fluorescence imaging (FI). Among these major imaging modalities, MRI has gained significant interest over the past several decades, due to its non-invasive nature, needless radioisotopes, high 3D resolution, and ability to distinguish multiple cell and tissue types [3,7–11]. Recently, MRI imaging has also played a substantial role

* Corresponding author.
E-mail address: sxy.wu@utoronto.ca (X.Y. Wu).
[1] Authors contributed equally to the work presented in this paper.

https://doi.org/10.1016/j.mtbio.2024.100954
Received 22 October 2023; Received in revised form 22 December 2023; Accepted 13 January 2024
Available online 17 January 2024

in the development of new cutting-edge theragnostic technologies, such as MRI-guided radiation therapy (MRIgRT). This next-generation technology has enabled radiation oncologists to perform real-time tumor imaging before and during RT [12], circumventing the need for multiple imaging sessions, enhancing precision RT, and reducing off-target radiotoxicity in patients [12–15].

However, MRI still requires the use of contrast agents to increase signal contrast. For this purpose, gadolinium (Gd)-based contrast agents (GBCAs) are commonly employed for MRI. The Gd^{3+} ion has unique paramagnetic properties which allow GBCAs to exhibit strong T1-weighted signal enhancement [16–18]. However, in recent years studies have revealed the release of free unchelated Gd^{3+} ions from GBCAs, increasing Gd-toxicity and leading to undesirable depositions in sites such as the brain and bone [19,20]. Moreover, lanthanides such as Gd are primarily excreted from the body through glomerular filtration, which at times may lead to precipitation in tissues and major organs [20–23]. These factors raise additional safety concerns in patients already undergoing exposure to toxic agents during cancer treatment, especially in patients with renal injury or other disease states, given the known association between the use of GBCAs in patients with renal failure and nephrogenic systemic fibrosis, predominantly with Group I (linear chelates), and to a lesser extent with Group II (macrocyclic chelates) Gd contrast agents [20–27]. Additionally, the lack of tumor-specific accumulation and retention of these GBCAs results in rapid MR signal diminution within the tumor masses and a short imaging window. This presents challenges to high-resolution MRI or MRIgRT, during which longer MRI sessions for the generation of well-defined images of tumor masses are needed for better treatment planning and RT delivery [28–31]. As a result, multiple doses of the contrast agents may be required to maintain the MR signal duration and intensity during the imaging sessions, which further increases the concern of Gd accumulation and toxicities in compromised patients [21,32,33].

To address such shortcomings, manganese (Mn)-based contrast agents (MBCAs) have been developed including various Mn formulations ranging from free $MnCl_2$ solution, Mn-complexes, and Mn-containing nanoparticles [34,35]. Mn is a natural cellular constituent and exhibits a better biosafety profile than Gd [32,36,37]. At the biological level, Mn is a co-factor of multiple enzymes and is crucially involved in enzymatic reactions, particularly concerning mitochondrial function [32,38]. While Gd is excreted through glomerular filtration, Mn is cleared through hepatobiliary excretion via bile acids and is more effectively metabolized and excreted through this mechanism [20,38–40]. Bivalent Mn^{2+} ion works similarly to other paramagnetic ions such as Gd^{3+} and can effectively increase the T_1-weighted MRI signal intensity [7,37]. Furthermore, MBCAs exhibit superior capability of enhancing MR contrast signal in tumors owing to higher cellular uptake and relaxivity over GBCAs, with Mn^{2+} ions being preferentially taken up by cancerous cells with high expression of calcium receptors over normal cells [4,35,41]. These characteristics make MBCAs more promising alternatives than conventional GBCAs for clinical applications [34,42]. So far, a few non-nanoparticulate MBCA products, such as oral $MnCl_2$ solution (LumenHance®) and chelated Mn-complex Mn-DPDP (Teslascan®), have been approved for clinical use. However, the rapid renal clearance and lack of tumor specificity limit their clinical utility and raise concerns about their potential adverse effect on normal tissues [32,43–46]. Given these factors and low demand for use in the detection of hepatobiliary tumors, Teslascan® was withdrawn by the manufacturer in 2003 from the US and in 2012 from Europe markets. Therefore, nanoparticulate formulations with tumor-specific accumulation and tumor microenvironment-responsive properties are desirable to mitigate these concerns [32,47].

Herein, we have designed a novel biocompatible and intravenously (IV) injectable manganese dioxide (MnO_2)-based nanoparticulate MBCA using pharmaceutically acceptable lipids and polymer to warrant biocompatibility and future development for clinical application. In previous work, we reported first-handedly that MnO_2-loaded nanoparticles were able to react with H_2O_2 in hypoxic and acidic tumors, producing O_2 *in situ* and enhancing radiotherapy in various tumor models [48–52]. Based on these findings, we reformulated and optimized the formulation of MnO_2-encapsulated terpolymer-lipid nanoparticles (TPL-MDNPs) and developed a scalable manufacturing process (Fig. 1A) to enhance tumor-specific T1W MR-contrast enhancement for precise cancer diagnosis and potential MRIgRT. The incorporated terpolymer, which consists of polysorbate-80 (PS80) and poly(methacrylic acid) (PMAA)-grafted starch, enables the recruitment of circulating apolipoproteins such as ApoE, leading to increased TPL-MDNPs tumor cell uptake and tumor penetration via low-density lipid receptor (LDLR)-mediated transcytosis into peripheral and intracranial tumors [53–56]. The bioreactive TPL-MDNPs react with the tumor by-product, reactive oxygen species (ROS) H_2O_2 in the tumor sites to produce paramagnetic Mn^{2+} ions, thereby enhancing localized tumoral MRI signal (Fig. 1B). In addition, the carboxylic groups in the PMAA bind with free Mn^{2+} ions by ionic complexation, leading to the effective reduction of their toxicity and amplification of the MRI-contrast enhancement in comparison to free ionic formulation [49,57].

In this work, we performed a comprehensive evaluation of the physicochemical properties of the TPL-MDNPs before and after terminal sterilization and the effect of lyophilization condition on their long-term storage stability. We then studied their application in MRI signal enhancement, *in vitro* and *in vivo* biocompatibility, and organ distribution and clearance profiles. The results demonstrated excellent colloidal properties and biocompatibility, as well as strong T_1-weighted relaxivity in response to tumor tissue-relevant H_2O_2 levels *in vitro*. *In vivo* MRI studies using various orthotopic tumor models of brain, breast, prostate, and pancreas cancers revealed higher effectiveness and selectivity of TPL-MDNPs for tumor-specific MR-contrast enhancement compared to clinically used GBCA (Gadovist®1.0, Group II macrocyclic GBCA) at the equivalent concentration. Furthermore, remarkable improvements in prolonged T1W tumor MR-contrast enhancement were achieved as demonstrated in brain and breast tumors with single IV administration of TPL-MDNPs compared to Gadovist®1.0. Overall, the results of this work suggest that the TPL-MDNP is promising as a next-generation MBCA to address the unmet need for biocompatible and tumor-responsive MRI contrast agents.

2. Results and discussion

2.1. Synthesis and physicochemical characterization of TPL-MDNPs

TPL-MDNPs were synthesized as previously described, with modifications to optimize scalable production (Fig. 1) [57,58]. Transmission electron microscopy images of TPL-MDNPs revealed the lyophilized NPs have a near-spherical structure with a compact overall morphology (Fig. 2A). The size, ζ –potential, T_1-weighted relaxivity (T_1_Rel) (with or without H_2O_2), and osmolarity in 5 % dextrose are tabulated in Fig. 2B. A negative ζ-potential value of -30 ± 5 mV allows TPL-MDNPs to stabilize in aqueous solution via intra-nanoparticulate electrostatic repulsion. After terminal γ-ray sterilization at 20–30 Gy under ice, TPL-MDNPs resuspended in aqueous solution maintained identical hydrodynamic size at 27 ± 3 °C (Fig. S1). A gel-blot test result of the sterilized samples demonstrated formulations to be well below US Pharmacopeia (USP) bacterial endotoxin standards for aqueous injectables of 0.5 EU/mL [59], indicating the present formulation can be safely sterilized to meet the regulatory standards while maintaining the desirable physicochemical properties.

The reduction of $KMnO_4$ to MnO_2 was investigated using UV–vis spectroscopy, revealing the characteristic MnO_2 broad absorbance peak at approximately 300–360 nm (Fig. S2). The composition of TPL-MDNPs was revealed using X-ray photoelectron spectrometry (XPS), and X-ray diffraction (XRD). The XPS Mn2p spectra for the MnO_2 precursor and the TPL-MDNPs showed a binding energy difference (ΔE) of 11.8 eV

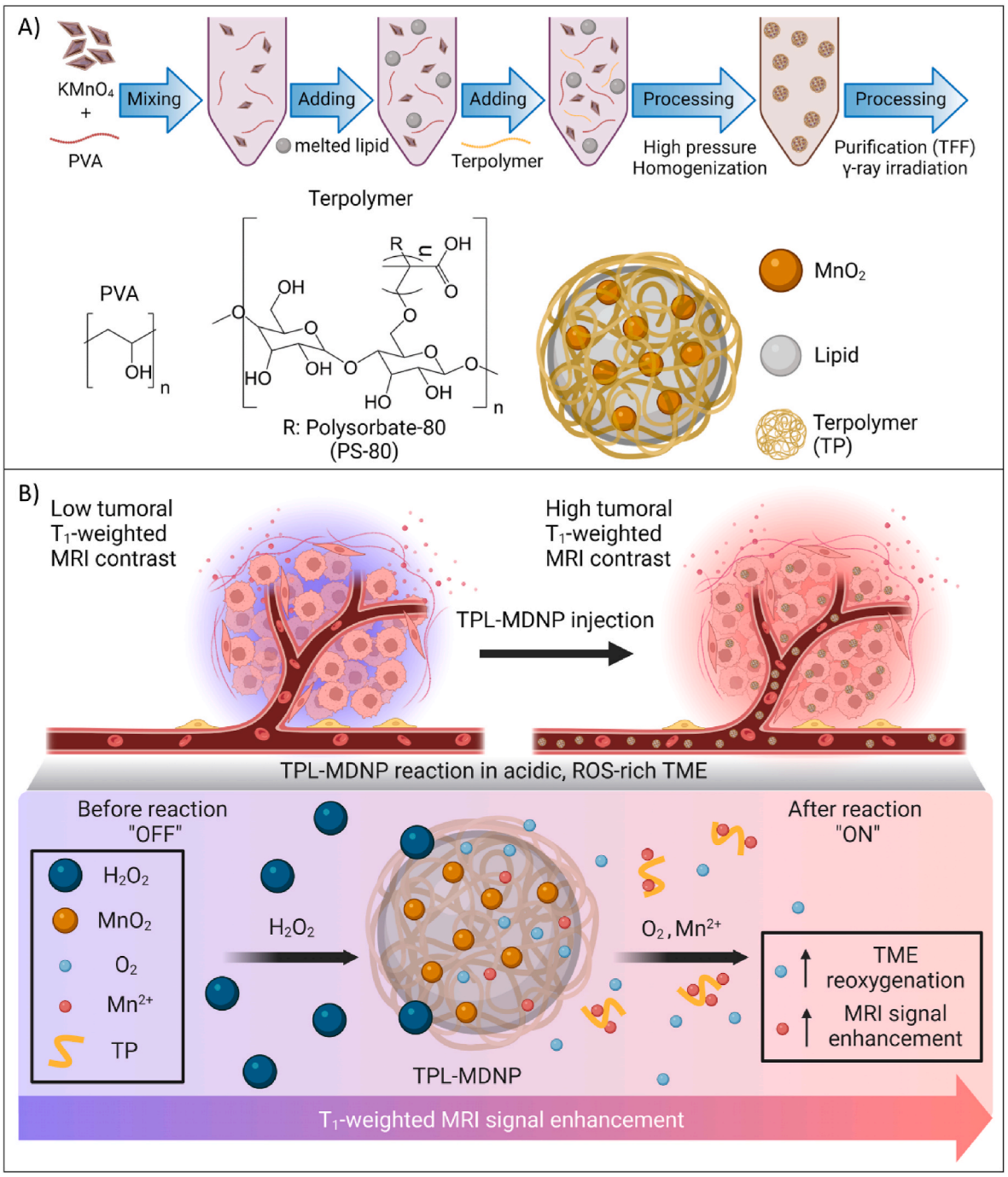

Fig. 1. A) Schematic representation of the TPL-MDNPs synthesis via reduction of $KMnO_4$ to MnO_2 and the use of oil-in-water self-emulsion method for MnO_2-loaded terpolymer-lipid matrix formation into the TPL matrix. B) Schematic illustration of MnO_2 conversion to Mn^{2+} and O_2 in hypoxic tumor microenvironment for MRI enhancement. The Mn^{2+} ions generated *via* the reaction of MnO_2 with H_2O_2 in the acidic TME are complexed with the carboxylic groups of the polymer, increasing MR contrast while reducing Mn toxicity.

between the $Mn2p_{1/2}$ and $Mn2p_{3/2}$ peaks, which corresponded to the presence of MnO_2 in TPL-MDNPs (Fig. 2C). Finally, the XRD spectra of MnO_2 precursor and TPL-MDNPs indicated a lack of characteristic peaks in the range of 30° and 70°, which confirmed that MnO_2 was in amorphous form (Fig. S4).

The stability of lyophilized TPL-MDNPs stored under various conditions for different time points was investigated as outlined in the FDA standard protocol for intermediate and long-term storage of pharmaceutical products [60]. Samples packed in type-1 glass vials under vacuum, atmospheric, or N_2 conditions and stored at 5 ± 3 °C demonstrated similar physiochemical characteristics up to 6 months of storage when compared to 0-day pre-storage samples (Fig. 2D and E, and S5). There was no observed change in particle size up to 7 days post reconstitution when stored at 5 ± 3 °C. Together these results demonstrated TPL-MDNPs have excellent long-term storage stability at refrigerated conditions, which is easily achievable in clinical settings where refrigeration is available.

Cancer cells can generate H_2O_2 at rates of up to 0.5 nmol/10^4 cells/h due to enhanced mitochondrial activity and dysregulation of oxidative enzymes, resulting in the elevation of H_2O_2 levels within the hypoxic TME [50,61–63]. Exploiting differences in H_2O_2 levels between diseased and non-diseased tissues, the reaction of TPL-MDNPs with H_2O_2 thus

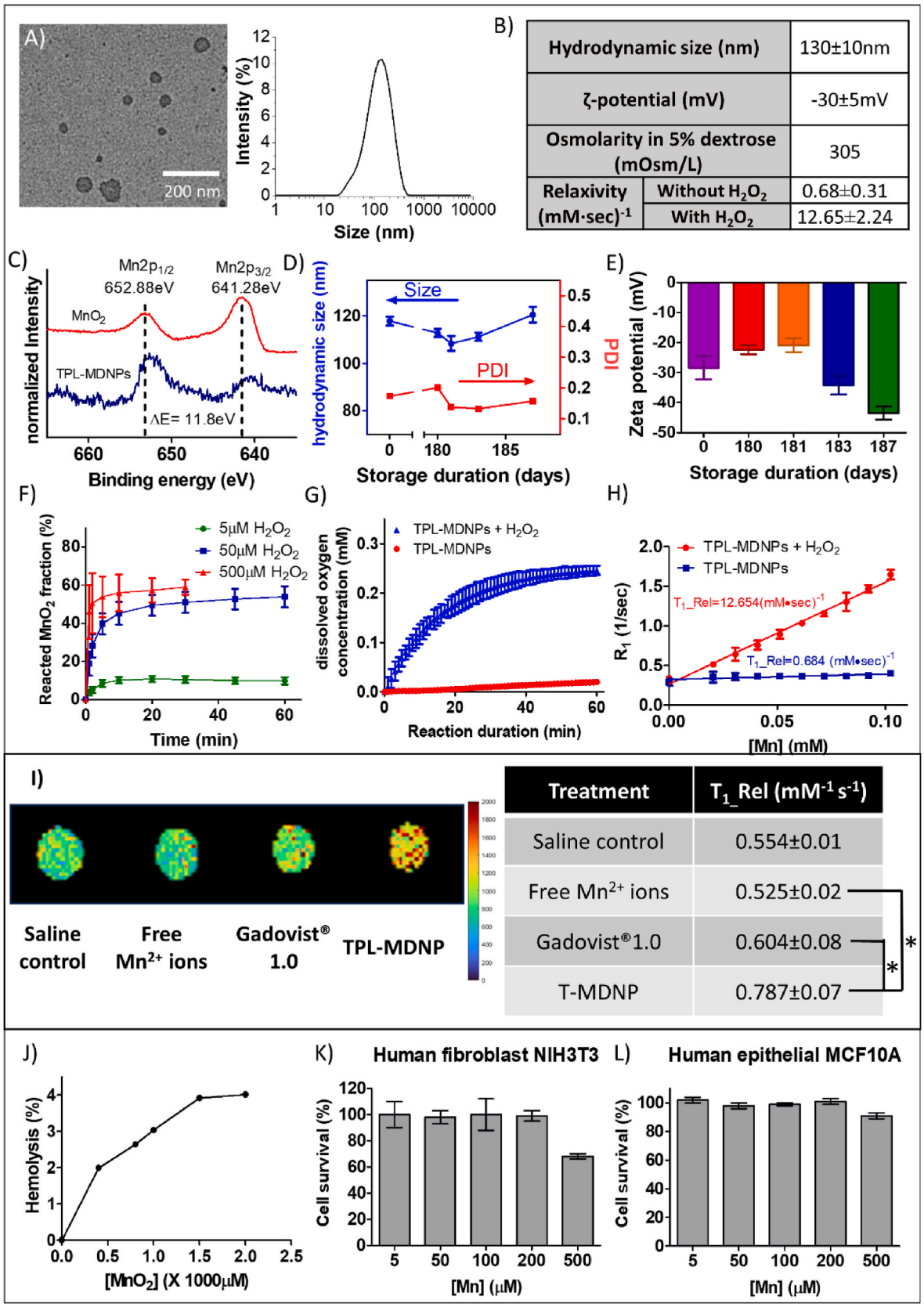

(caption on next page)

Fig. 2. Physio-chemical characterization, *in vitro* hemolysis, cytotoxicity, and cellular uptake of TPL-MDNPs. A) Representative TEM image and DLS size distribution of synthesized TPL-MDNPs. Scale bar = 200 μm. B) Table summarizes the major physicochemical properties of TPL-MDNPs, including hydrodynamic size, ζ-potential, osmolarity, and T_1_Rel under 1.5 T MRI of optimized IV injectable formulation in 5 % dextrose. C) XPS Mn2p spectra of MnO_2 and TPL-MDNPs. D) Long-term storage hydrodynamic size and E) ζ-potential of lyophilized TPL-MDNPs under refrigerated temperature (5 ± 3 °C) in vacuum-sealed vials. F) *In vitro* fraction of reacted MnO_2 (initial MnO_2 concentration = 100 μM) analysis within 60 min of reaction time with different concentrations of H_2O_2 at ambient temperature (approximately 27 ± 3 °C). The selected H_2O_2 concentrations of 5 μM and 50 μM simulate physiological levels of ROS found within healthy and tumoral tissues, respectively. G) *In vitro* dissolved oxygen generation of 100 μM TPL-MDNPs with and without 500 μM H_2O_2 at 27 ± 3 °C. H) T_1_Rel of 100 μM of TPL-MDNPs with and without the 500 μM of H_2O_2 after 1 h incubation in 37 °C aqueous environment under 1.5 T MRI. I) Cellular R_1 maps and T_1_Rel of U87MG-luc cells *in vitro* after incubation with different treatments for 4 h. J) *In vitro* hemolysis analysis of TPL-MDNPs in healthy Sprague Dawley rat RBC sample. K) *In vitro* toxicity of TPL-MDNPs against human fibroblast NIH3T3 cells (mean ± S.D., n = 6) and L) human epithelial MCF10A cells (mean ± S.D., n = 6). Cell survival (%) was assessed by MTT assay and is relative to the untreated group. Results are presented as mean ± S.D., n = 3.

acts to differentiate tumoral and healthy tissues based on MRI signal intensities. To understand the responsiveness of TPL-MDNPs to H_2O_2, *in vitro* reactivity rates of these NPs to different H_2O_2 concentrations were performed and measured as a function of absorbance changes over 60 min using UV–Vis spectroscopy (Fig. 2F). At the physiologic concentration of H_2O_2 (5 μM), TPL-MDNPs (100 μM of MnO_2) exhibited absorbance changes translating to approximately 10 % of TPL-MDNPs capacity reacting within 60 min. By comparison at a pathophysiological concentration of H_2O_2 (50 μM), TPL-MDNPs exhibited a rapid absorbance change translating to approximately 60 % of TPL-MDNPs capacity reacting within 60 min. In an anoxic environment, TPL-MDNPs continuously generated oxygen *in vitro* over 60 min in the presence of H_2O_2 (500 μM), while no oxygen was generated in the absence of H_2O_2 (Fig. 2G). *In vitro* T_1-weighted relaxivity (T_1_Rel) of TPL-MDNPs after complete reaction with H_2O_2 (500 μM) and in the absence of H_2O_2 was calculated to be 12.65 ± 2.24 $(mM{\cdot}sec)^{-1}$ and 0.68 ± 0.31 $(mM{\cdot}sec)^{-1}$, respectively under 1.5 T MRI (Fig. 2H). With the measured T_2-weighted relaxivity (T_2_Rel) of 17.18 ± 3.42 $(mM{\cdot}sec)^{-1}$ in the presence of H_2O_2 under the same magnetic field strength, the calculated R1/R2 ratio of the TPL-MDNP is 1.36. This value is close to the values of clinically used GBCAs at 1.5 T, making it an ideal contrast agent with high T_1-contrast enhancement capability [64]. The generation of paramagnetic Mn^{2+} ions resulted in up to 18.5-fold MRI signal enhancement compared to unreacted TPL-MDNPs, higher than the majority of GBCAs currently in clinical use, which range from 4.1 to 6.9 $(mM{\cdot}sec)^{-1}$ [64,65]. This improvement in T_1-weighted MR-contrast enhancement was further validated *in vitro* using human U87MG-luc glioblastoma cells treated with saline, free Mn^{2+} ions in $MnCl_2$ solution, Gadovist®1.0 (100 μM Gd) or TPL-MDNPs (100 μM Mn) with 50 μM H_2O_2 for 4 h. The cellular T_1_Rel treated with TPL-MDNP was 0.787 $mM^{-1}sec^{-1}$, which was 1.30-fold higher compared to Gadovist®1.0 at an equivalent dose (0.604 $mM^{-1}sec^{-1}$) (Fig. 2I). Additionally, treatment with TPL-MDNP exhibited notable signal enhancement in comparison to treatment with $MnCl_2$ solution (free Mn^{2+} ion) at equivalent Mn concentration, demonstrating improved cellular uptake of Mn through the nanoparticulate formulation. These results indicate that the TPL-MDNPs can effectively improve the MnO_2 cellular uptake and generate Mn^{2+} ions preferentially at higher rates and quantity in the ROS-rich TME for disease-state differential T1W MR signal enhancement [49].

2.2. In vitro osmolarity, hemolysis, and biocompatibility studies of TPL-MDNPs

The osmolarities of TPL-MDNPs in different suspensions were investigated to develop and optimize an injection formulation suitable for safe intravenous (IV) applications (Fig. S7). Changes in osmolarity as little as 1 % can cause antidiuretic hormone secretion, which in turn disrupts fluid homeostasis and may further compromise patients [66]. TPL-MDNPs suspended in 5 % dextrose has an osmolarity of 305 mOsm/L, closely resembling the osmolarity of plasma (300 mOsm/L) and was thus selected as the IV formulation used for all *in vivo* studies in this work [67]. In addition to osmolarity, hemocompatibility study is another critical component of the development of the IV formulation. The hemolytic analysis is used to determine the biocompatibility and pharmacological safety of the red blood cells (RBCs), where IV injectables would be considered "non-hemolytic" if *in vitro* percent hemolysis is below 25 % following the injection [68]. TPL-MDNPs in 5 % dextrose and other TPL-MDNP/solvents formulations with up to 2.0 mM of MnO_2 treated for 1 h at ambient temperature (approximately 27 ± 3 °C) caused hemolysis in approximately 5 % of RBCs obtained from healthy Sprague Dawley rats (Fig. 2J). TPL-MDNPs did not induce significant toxicity in non-tumorigenic human epithelial MCF10A and fibroblast NIH3T3 cells when treated for 24 h up to the concentration of 200 μM of MnO_2. (Fig. 2K and L). Confocal microscopy images of human brain U87MG, prostate PC3, and breast MDA-MB-231-luc-D3H2LN cell lines treated with Cy5-labeled TPL-MDNPs exhibited green cytoplasmic fluorescence after 1-h incubation, suggesting excellent *in vitro* cellular uptake of TPL-MDNPs in these cancer cell lines (Fig. S8).

2.3. In vivo tumoral MRI enhancement efficacy in tumor-bearing models

For clinicians to accurately evaluate tumor progression and establish precise treatment plans, MRI images must exhibit clear tumor delineation for precise control over local regional delivery of anti-cancer RT [14]. Given their relative area, T_1-weighted proton MR signal enhancement by TPL-MDNPs was initially visualized in human U87MG brain, human MDA-MB-231-D3H2LN breast, and patient-derived xenograft pancreatic cancer tumor-bearing mouse models and human PC3 prostate tumor-bearing rat models using a 7 T scanner to demonstrate the NP's capability to delineate tumor metastases. After 15 min post-IV injection of TPL-MDNPs at a dose of 70 μmol Mn/kg body weight for mice and 35 μmol Mn/kg body weight for rats, T1-weighted MR images in all models demonstrated strong tumor-related T_1 MR enhancement with well-defined outlines and clear delineation (Fig. 3). Interestingly, the MRI image generated using TPL-MDNPs showed an additional tumoral structure superior to the main tumor mass in patient-derived xenograft (PDX) pancreatic tumor-bearing mice model 15 min post-administration, which was absent from the image generated using Gadovist®1.0 (gadobutrol, Leverkusen, Germany). This difference in structured detail seen in these images may be related to enhanced penetration and retention (EPR) effects of nanostructured TPL-MDNPs and related to altered transporter expression. For example, within hypoxic tumors, hypoxia-inducible factor 1α (HIF1α) upregulation has been shown to drive the expression of divalent metal transporters in cancer cells, which can actively take up and distribute Mn^{2+} ions within the tumor mass, resulting in improved tumor delineation and diagnostic quality [69,70].

In vivo uptake of TPL-MDNPs was also investigated in human U87MG brain and human MDA-MB-231-D3H2LN breast mouse tumor models using *in vivo* bioluminescence and fluorescence imaging to understand tumor uptake efficacy of the NPs in solid tumors. Indocyanine green (ICG)-labeled TPL-MDNPs (70 μmol Mn/kg) demonstrated increased ICG–dependent fluorescence uptake in both U87MG and MDA-MB-231-luc-D3H2LN tumor metastases 2 h post-injection (Fig. 4A and B, and S9). *Ex vivo* images of harvested brain tissue at 2 h post-administration further confirmed co-localization of ICG fluorescence and luciferase-dependent bioluminescence in expressing U87MG tumor masses, demonstrating tumor uptake and retention of TPL-MDNPs.

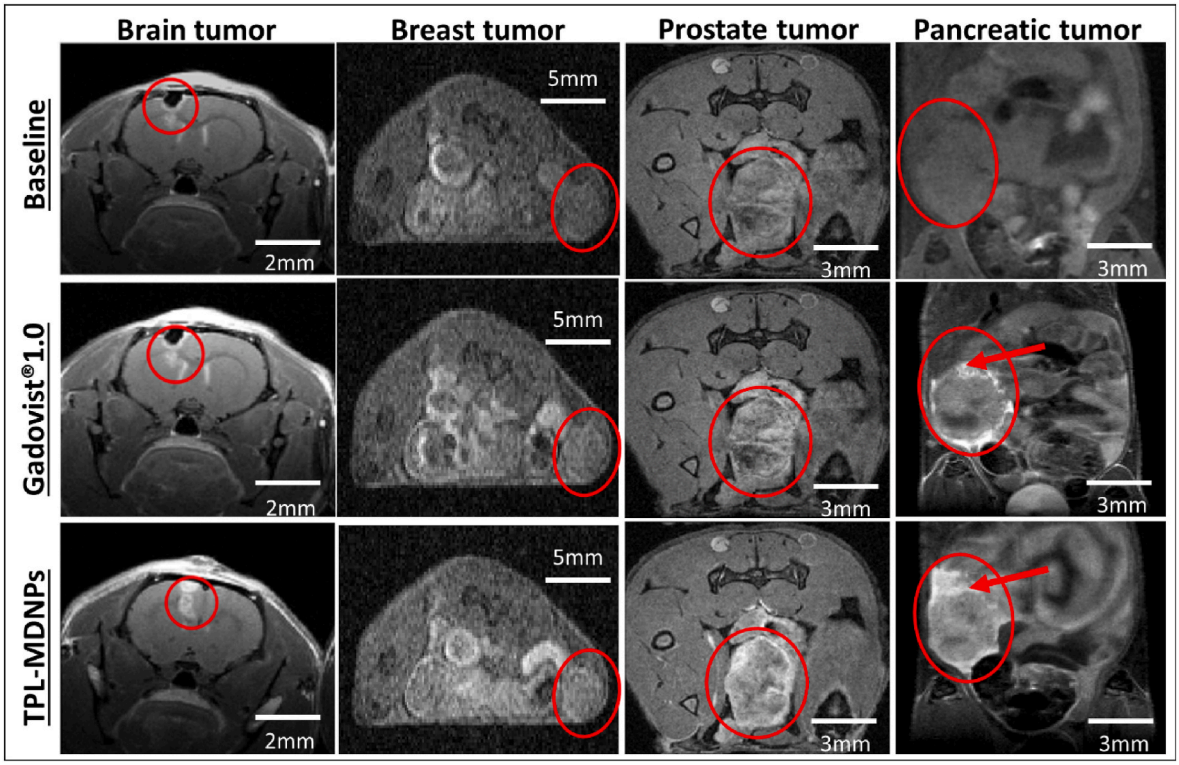

Fig. 3. *In vivo* T1-weighted MRI images (TR = 1000 msec) of orthotopic human U87MG glioblastoma (mice), human MDA-MB-231-D3H2LN breast tumor (mice), human PC3 prostate tumor (rats), or patient-derived pancreatic tumor xenografts (PDX) (mice) at baseline (prior to contrast agent injection) and 15 min following a single TPL-MDNPs or Gadovist®1.0 IV injection at 70 μmol Mn/kg animal weight for mice and 35 μmol Mn/kg animal weight for rats. Circled areas indicate target tumor masses of the corresponding tumors. The red arrows on the MRI images of PDX pancreatic tumor models indicate the distinct tumor structure that was presented only in the TPL-MDNP-administered group and absent in the Gadovist®1.0-administered group superior to the pancreatic tumor mass visible in both contrast agent groups. (For interpretation of the references to color in this figure legend, the reader is referred to the Web version of this article.)

To investigate the potential enhancement of T1W MR signal by TPL-MDNPs in comparison to Gadovist®1.0, a single dose of TPL-MDNPs or Gadovist®1.0 was injected at a dose of 70 μmol/kg into mouse models previously transplanted with human brain U87MG-luc or human breast MDA-MB-231-D3H2LN cells and T1W 7 T MR signals measured up to 1 h post-injection. Comparison of T_1-weighted relaxation rate ($R_1 = 1/T_1$) between TPL-MDNPs and Gadovist®1.0-injected models showed observable difference at 5 min post-injection, with significant MRI signal enhancements at 30- and 60-min post-injection (Fig. 4C and D). Strikingly, at the 60-min post-injection timepoint, signal enhancement of TPL-MDNPs was maintained at more than 2-fold the level obtained from Gadovist®1.0 at the same time point. Additionally, a single dose of TPL-MDNPs at 70 μmol Mn/kg was observed to generate well-defined tumor outlines in breast and brain tumor-bearing animal models 15 min following IV injection at 30 % less than the recommended clinical dose for Gadovist®1.0 at 100 μmol Gd/kg [27]. The observed increases in T1W MRI enhancement intensity and duration by TPL-MDNPs at a lower dosage compared to Gadovist®1.0 are likely due to the difference in the formulation of the respective contrast agents. The EPR effect, driven by the nanoparticular property of TPL-MDNPs, allows them to penetrate and get retained more effectively within the tumor masses, which are characterized by irregular vasculatures and high interstitial fluid pressure that often discourage the retention of many pharmaceutics [71–73]. Gadovist®1.0, on the other hand, is a chelated macrocyclic GBCA formulation that lacks the means for tumor-specific uptake or retention and, thus, is rapidly cleared from the tumors [31,74]. This leads to rapid MR signal reduction and the need for multiple injections for signal maintenance, which further exacerbates the potential Gd-related accumulation and toxicity. In contrast, the use of TPL-MDNPs is beneficial for longer MRI sessions where more time and detailed MRI images are requested for the treatment delivery and planning, effectively eliminating the need for signal maintenance, and reducing the risks of toxicity.

2.4. Pharmacokinetic analysis and tissue clearance of TPL-MDNPs in healthy murine models

Conventional GBCAs have been reported for their Gd-related accumulations and toxicities that have raised concerns and restricted their uses in compromised patients [16,19,20,23,75,76]. To understand the clearance profile of TPL-MDNPs, pharmacokinetic (PK) analysis of TPL-MDNPs was performed by measuring Mn concentration in blood plasma using inductively coupled plasma-optical emission spectrometry (ICP-OES) up to 24 h after a single injection of TPL-MDNPs (35.0 μmol Mn/kg) in healthy Sprague Dawley rats. Rats were selected over mice due to their higher blood volume, and an efficacious dose of 35.0 μmol Mn/kg was selected based on the weight-dependent conversion from mouse's lowest efficacious dose of 70 μmol Mn/kg [77]. Fig. 5A summarizes the PK parameters of TPL-MDNPs, fitted by the ADAPT5 PK modeling program to a two-compartment model based on the previous work [78]. The plasma elimination half-life ($t_{1/2\beta}$) of TPL-MDNPs in plasma was approximately 10.42 ± 1.68 h in healthy rats and is almost 7-fold longer than the clinically used GBCAs, with the elimination half-life of 1.5 h [31]. The total nanoparticle exposure over time ($AUC_{0-\infty}$) was 77.82 ± 4.11 μmol•h/L. The total plasma clearance (CL) was also calculated to be at approximately 0.1 L/h.

The tissue clearance of TPL-MDNPs (35.0 μmol Mn/kg injected) was confirmed by measuring the Mn concentration via *ex vivo* ICP-OES in major organs of healthy Sprague Dawley rats at 7 days post-injection. No significant difference in Mn levels in all organs between the TPL-MDNPs treated rats and the saline control rats was observed by 7 days (Fig. 5B). This observation was further confirmed by investigating in the changes

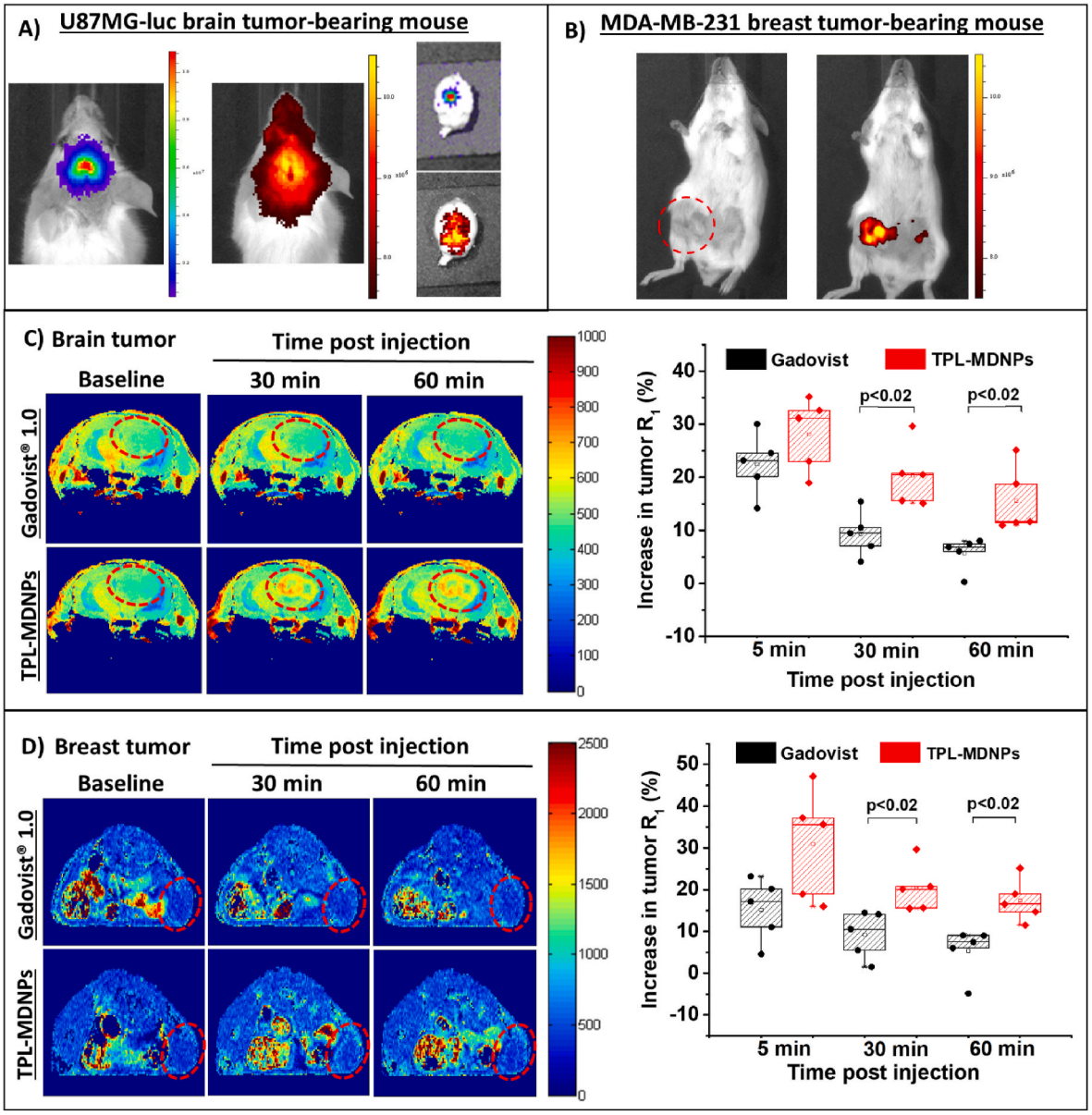

Fig. 4. *In vivo* tumoral uptake of ICG-labeled TPL-MDNPs in orthotopic human A) U87MG luciferase expressing (U87MG-luc) brain and B) MDA-MB-231-D3H2LN breast tumor-bearing mouse models. *Ex vivo* brain sample of the U87MG-luc tumor-bearing mouse is also presented (A). The rainbow map images represent the bioluminescence signal (luciferin) of the luciferase-expressing U87 tumor mass and the red-orange map represents the fluorescence signal (ICG) of the TPL-MDNPs. C) *In vivo* R_1 maps of brain U87-luc- and D) breast MDA-MB-231-luc-D3H2LN-bearing SCID mice at baseline, 30-, and 60-min post-injection with a single dose of TPL-MDNPs (70 μmol Mn/kg) or Gadovist®1.0 (70 μmol Gd/kg). The red dotted circles indicate the tumor masses. The corresponding bar graphs represent the changes in tumor R_1 over time in both tumor models that were calculated in reference to the baseline values. Results are presented as mean ± S.D. within the same cohort, n = 5 mice/group/model. (For interpretation of the references to color in this figure legend, the reader is referred to the Web version of this article.)

in R_1 values over 7 days in the organs of healthy SCID mice after a single injection of TPL-MDNPs at 70 μmol Mn/kg. Interestingly, greater than 80 % of the signal diminished from major organs within the first 24 h, indicating rapid clearance of TPL-MDNPs (Fig. 5C and D, and S10). Remarkably, unlike conventional lipid-based nanoparticles that tend to accumulate predominantly in the liver, the hybrid polymer-lipid-based TPL-MDNPs exhibited reduced liver uptake and fast clearance from the liver. At 4 h post-injection, the TPL-MDNPs-delivered Mn^{2+} in the liver was reduced by ~3-fold and returned to the baseline within 24 h, evidenced by the diminishing R_1 signal (ΔR_1) (Fig. 5C) [79]. No TPL-MDNP-related T1W signals were detected at one week post-single-dose injection, suggesting complete clearance of the NPs from the major organs during the first week of the post-injection period (Fig. 5D). Pharmacokinetics, tissue clearance, and tumor uptake indicate that NPs are delivered and retained in tumor masses following IV injection while exhibiting complete removal from these organs with minimal concerns for undesirable accumulation. These desired clearance profiles of TPL-MDNPs are most likely due to a combination of factors, including the surface properties and the particle size, contributing to ideal and favorable circulation time while preventing undesirable long-term accumulations and toxicities within major organs such as the liver, kidney, and brain [80,81].

2.5. *In vivo* dose escalation study of TPL-MDNPs

In vivo dose escalation studies were performed in healthy Sprague Dawley rats (6 weeks old) to identify any potential *in vivo* toxicity of TPL-MDNPs. Cardiovascular, liver, and renal function panels and

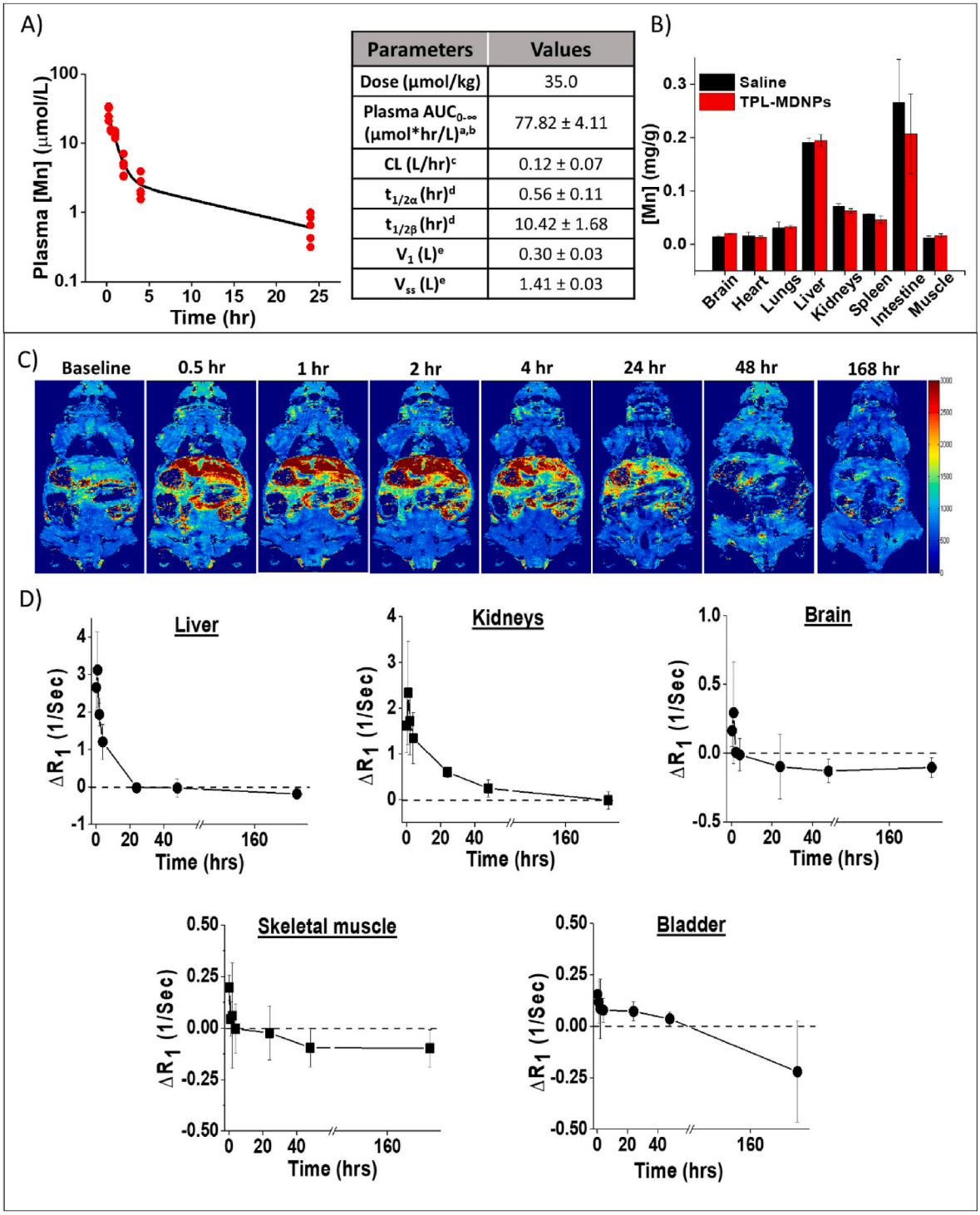

Parameters	Values
Dose (μmol/kg)	35.0
Plasma $AUC_{0-\infty}$ (μmol*hr/L)[a,b]	77.82 ± 4.11
CL (L/hr)[c]	0.12 ± 0.07
$t_{1/2\alpha}$ (hr)[d]	0.56 ± 0.11
$t_{1/2\beta}$ (hr)[d]	10.42 ± 1.68
V_1 (L)[e]	0.30 ± 0.03
V_{ss} (L)[e]	1.41 ± 0.03

Fig. 5. Pharmacokinetic (PK) profile of TPL-MDNPs in healthy Sprague Dawley rats and SCID mice. A) PK analysis of a single injection of TPL-MDNPs (35.0 μmol Mn/kg) in healthy Sprague Dawley rats (n = 5 mice). Mn plasma concentration (μmol Mn/L) was assessed over a period of 24 h post-injection. The table summarizes the mean PK parameters. [a]All data points were averaged to provide the mean, and the value was used for the calculations; AUC_{0-24h} was calculated by the trapezoidal rule. [b]The blood AUC was obtained from serum samples. $AUC_{0-\infty}$ was estimated by addition of AUC_{0-24h} to $AUC_{extrapolated}$ to infinity or (C_{24h}/β), where C_{24h} is the Mn concentration at 24 h and β is the terminal decay constant. [c]Total plasma clearance (CL) was calculated as dose/AUC. [d]$t_{1/2\alpha}$ represents the distribution half-life and $t_{1/2\beta}$ represents the elimination half-life. [e]V_{ss} is the volume of distribution at steady state and calculated according to $V_{ss} = V_1 \times (1 + k_{12}/k_{21})$ where V_1 is the volume of central compartment and k_{12} and k_{21} are micro-constants. B) *Ex vivo* ICP-OES Mn biodistribution analysis of TPL-MDNPs in major organs after 7 days post-injection coasting period (n = 5). C) *In vivo* MRI biodistribution images of TPL-MDNPs (70 μmol Mn/kg) over the 7 days post-injection coasting period in mice after a single IV injection. D) Analyses of MRI T1W signals for *in vivo* biodistribution in liver, kidneys, brain, bladder and skeletal muscle. Values were quantified for changes in R_1 values at different time points. Results are presented as mean ± S.D., n = 5 mice.

hematology were performed at a 2-week recovery period post-single-dose treatment of TPL-MDNPs at 300 μmol Mn/kg and multiple-dose treatment at 300 μmol Mn/kg per injection per week for a total of four weeks to investigate the NPs-related effects on systemic physiological functions of healthy rodents. The control group was injected with saline of equivalent volume. No significant changes were observed in all biomarkers between NP-treated and control groups following single- and multiple-dose treatment (Fig. 6A and B). Furthermore, all values were within accepted normal ranges when compared to published results of the vendor (Envigo, IN, USA), suggesting no TPL-MDNPs-related systemic toxicities in this rat model (Envigo, IN, USA).

Histopathology performed for major body organs following the 2-week recovery period post-treatment indicated no TPL-MDNPs induced toxicities and accumulation into major organs. These results further supported the non-toxic nature and rapid clearance of the TPL-MDNPs (data not shown)[17,22]. Additionally, no significant changes in

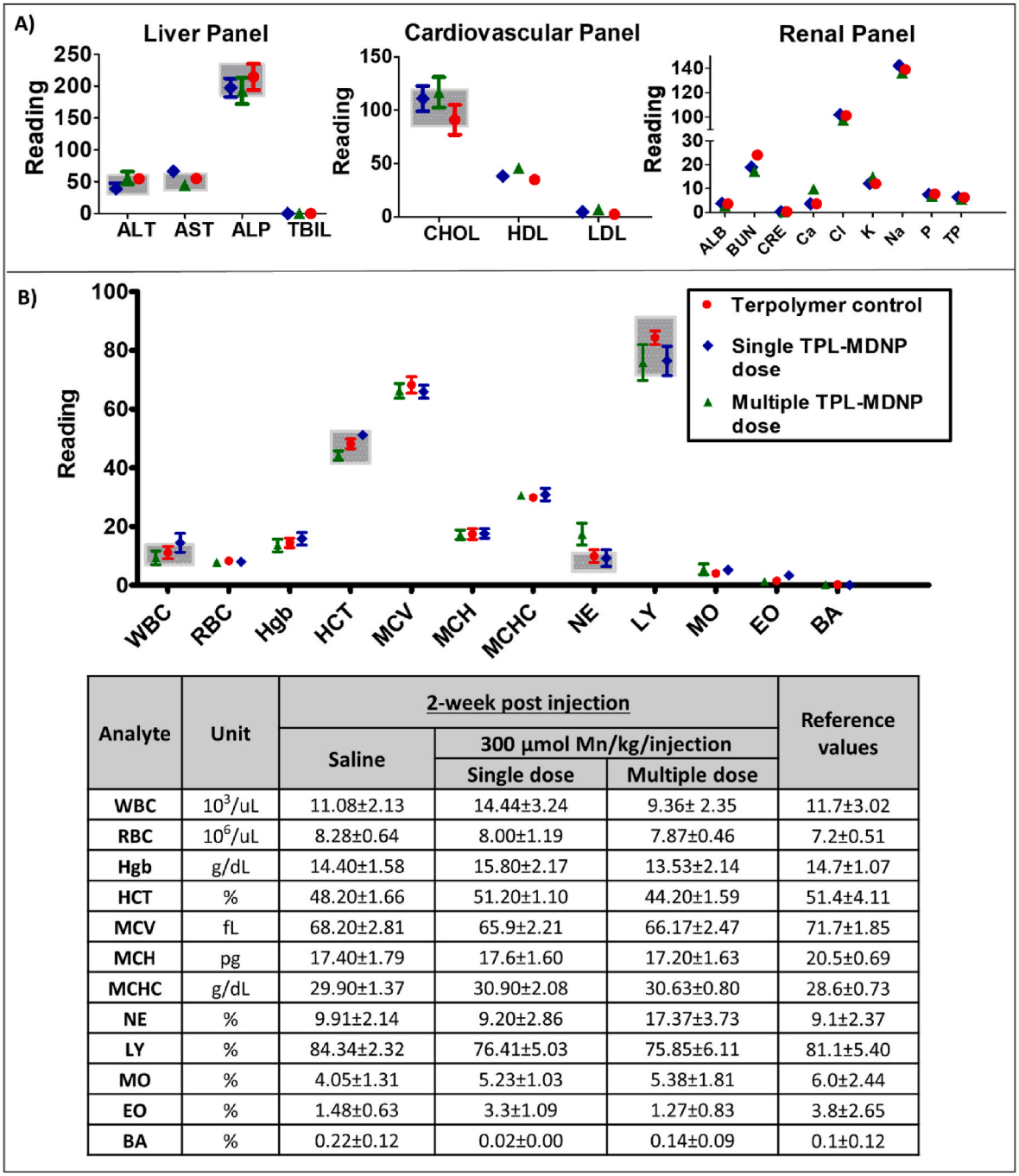

Analyte	Unit	2-week post injection			Reference values
		Saline	300 μmol Mn/kg/injection		
			Single dose	Multiple dose	
WBC	10^3/uL	11.08±2.13	14.44±3.24	9.36± 2.35	11.7±3.02
RBC	10^6/uL	8.28±0.64	8.00±1.19	7.87±0.46	7.2±0.51
Hgb	g/dL	14.40±1.58	15.80±2.17	13.53±2.14	14.7±1.07
HCT	%	48.20±1.66	51.20±1.10	44.20±1.59	51.4±4.11
MCV	fL	68.20±2.81	65.9±2.21	66.17±2.47	71.7±1.85
MCH	pg	17.40±1.79	17.6±1.60	17.20±1.63	20.5±0.69
MCHC	g/dL	29.90±1.37	30.90±2.08	30.63±0.80	28.6±0.73
NE	%	9.91±2.14	9.20±2.86	17.37±3.73	9.1±2.37
LY	%	84.34±2.32	76.41±5.03	75.85±6.11	81.1±5.40
MO	%	4.05±1.31	5.23±1.03	5.38±1.81	6.0±2.44
EO	%	1.48±0.63	3.3±1.09	1.27±0.83	3.8±2.65
BA	%	0.22±0.12	0.02±0.00	0.14±0.09	0.1±0.12

Fig. 6. *In vivo* biosafety studies in healthy Sprague Dawley rats (6–8 weeks old) treated with a single dose (300 μmol Mn/kg) or multiple doses (300 μmol Mn/kg per injection per week for a total of four weeks) of TPL-MDNPs. The control group was treated with saline at the same injection schedule as for TPL-MDNPs. Safety assessment performed following two weeks of post-treatment recovery period. A) clinical chemistry on cardiovascular, liver, and renal function panels and B) hematology panels were obtained at day 14 post IV injection (n = 5 rats). Reference values (as represented by the shaded bars) were obtained from published data of the vendor (6–8 weeks old, Envigo, IN, USA). In cardiovascular function panel, units of CHOL, HDL, and LDL are in mg/dL. In liver function panel, units of ALT, AST, and ALP are in U/L, and TBIL is in mg/dL. In the renal function panel, units of ALB and TP are in g/dL, BUN, CRE, Ca, and P are in mg/dL, and Cl, K, and Na are in mmol/L.

body weight (Fig. S11) and neurobehavioral abnormalities were observed (observation data not shown), confirming the biosafety feature of the TPL-MDNPs and supporting the potential utility of TPL-MDNPs as a safe alternative to GBCAs.

3. Conclusion

A next-generation MBCA, TPL-MDNP formulation has been successfully manufactured using a scalable "one-pot" method and its suitability for precise tumor delineation and tumor-specific MR signal enhancement has been demonstrated. The final product exhibits excellent stability after standard sterilization and long-term storage, a desirable pharmaceutical property for safe clinical translation of nanotheragnostic. The tumor-selective accumulation and reactivity of TPL-MDNPs render the stronger T1W MRI contrast enhancement and delineation of tumor masses than surrounding healthy tissues which cannot be offered by clinically used GBCAs. The higher intensity and longer duration of T1W MR tumor signal generated by intravenously injected TPL-MDNPs present a unique advantage over existing GBCAs in reducing multiple dosing for detailed MRI and especially for MRIgRT. The excellent biosafety and clearance profiles observed in the studied murine models warrant further development of this new nanoparticulate MBCA for clinical applications.

4. Experimental methods

4.1. Materials

Soluble corn starch (MW = 11,000 g/mol), methacrylic acid (MAA), sodium thiosulfate (STS), potassium persulfate (KPS), polysorbate 80 (PS80), sodium dodecyl sulfate (SDS), N-(3-(Dimethylaminopropyl)-N′-ethylcarbodiimide hydrochloride (EDC), 3-(4,5-dimethyl-2-thiazolyl)-2,5-diphenyl-2H-tetrazolium bromide (MTT), ethyl arachidate, dihydroethidium (DHE), polyvinyl alcohol (PVA), hydrogen peroxide solution (30 wt % in H_2O, H_2O_2), dextrose, phosphate-buffered saline (PBS), Triton X-100, and Bovine Serum Albumin (BSA) were purchased from Sigma-Aldrich (Oakville, ON, Canada). Cyanine 5.5 amine (Cy5.5) was purchased from Lumiprobe (Hunt Valley, MD, USA). All chemicals were of analytical grade and used without further purification if not indicated otherwise.

4.2. Preparation and characterization of TPL-MDNPs

TPL-MDNPs were prepared using an oil-in-water emulsion method as described previously by our group and optimized for scalable production of TPL-MDNPs (Fig. 1A) [57,58]. Briefly, the crude inorganic MnO_2 NP-lipid nanoconstructs were first synthesized via the reduction of $KMnO_4$ to MnO_2 in the presence of poly(vinyl alcohol) (PVA) in an aqueous medium, followed by the addition of ethanolic solution of phospholipid (DPPC) and cholesterol. The emulsion was then mixed with biocompatible terpolymer (TPL), during which the hydrophobic interaction between the TPL and the lipid domain of the nanoconstructs led to the self-assembly and formation of TPL-MDNPs. The emulsion was then passed through a high-pressure homogenizer at a pressure above 20 Kpsi to produce small NPs. The final product was collected in ice-cold water, filtered, and purified using tangential flow filtration (TFF) to remove the unreacted reagents. The purified solution was lyophilized in the presence of sucrose as a cryo-protectant agent. The final lyophilized product was stored in sealed type-1 glass vials. Dynamic light scattering (DLS) and ζ-potential measurement of resuspended TPL-MDNPs in filtered, deionized, and distilled water (ddiH_2O) was carried out for hydrodynamic size, PDI, and ζ-potential of the finalized product using Malvern Zetasizer Nano ZS (Malvern Panalytical, Malvern, UK). Terminal sterilization of lyophilized samples was performed using γ-ray at a dose of 20–30 kGy. The completion of $KMnO_4$ conversion to MnO_2-NP and self-assembly into the TPL-MDNPs was confirmed by ultraviolet–visible (UV–vis) spectrophotometry (Aligent Technologies, California, USA), XPS, and XRD (Thermofisher Scientific, Massachusetts, USA). Limulus Amebocyte Lysate (LAL) test for endotoxin analysis of the γ-ray sterilized TPL-MDNPs was performed using via gel-clot method for confirmation of sterilization [59], and DLS and ζ-potential measurements were carried out to investigate sterilized samples stability.

4.3. Storage stability of TPL-MDNPs

The long-term storage stability of the TPL-MDNPs was investigated at 1, 3, and 6 months after lyophilization. The lyophilized TPL-MDNPs were stored at either room (25 ± 3 °C) or refrigerated (5 ± 3 °C) environmental temperature, and under normal room air, nitrogen, or vacuum conditions. Samples were prepared from the stored NPs at 1, 3, and 6 months by resuspending them in filtered 5 % dextrose aqueous solution, and hydrodynamic size, PDI, and ζ-potential of the reconstituted samples were measured 7 days consecutively using Malvern Zetasizer Nano ZS.

4.4. In vitro relaxivity analysis of TPL-MDNPs

TPL-MDNPs at concentrations ranging from 0.01 to 0.2 mM were prepared by suspending lyophilized samples with 0.1 % saline, and then 100 μL of each sample were transferred into each well of 96-well plates. 100 μL of 1 mM H_2O_2 was then added into each well to reach a final concentration of 500 μM (n = 3 for each concentration). For negative saline controls, 100 μL of 0.1 % saline was added into each well (n = 3 for each concentration). The plate was then allowed to react for 1 h at 37 °C to ensure complete TPL-MDNPs conversion to paramagnetic Mn^{2+} before measurement of the T1W MRI signal. T_1_Rel was then assessed for samples within the 96-well plates at both 1.5 and 7 T (1.5 T Aera, Siemens Corporation, Erlangen, DE; 7 T Bio-Spec, Bruker Corporation, Ettlingen, DE). For the 1.5T Aera, the well-plate was sandwiched between 2 special-purpose 4-element array coils (Siemens Corporation). An extra well plate filled fully with water was included to enable system tuning and matching. Both T_1 and T_2 mapping acquisitions shared common geometric features (12 × 12 cm field-of-view; 128 x 128 matrix; 0.9 mm in-plane resolution; 5 mm slice thickness). T2 mapping used a multi-echo spin-echo technique (32 echoes ranging from echo times (TE) of 10–320 msec; repetition time (TR) of 4000 msec; 275 Hz/pixel readout bandwidth; 4/8 partial Fourier factor; 9 min 10 s. T_1 mapping used a variable TR spin-echo approach (TE 15 msec; TR 30, 50, 100, 150, 250, 500, 750, 1000, 1500, 2000, 2500, 4000 msec; 130 Hz/pixel readout bandwidth; 29 min 4 s). The 7T Bio-Spec was equipped with the B-GA20S gradient coil, 15.5 cm inner diameter quadrature volume resonator for RF transmit and receive, and the geometric features of the acquisitions were shared (11 × 8 cm field-of-view; 220 x 160 matrix; 0.5 x 0.5 in-plane resolution; 5 mm slice thickness). T_2 mapping used a multi-echo spin-echo technique (30 echoes ranging from echo times (TE) of 10–300 msec; repetition time (TR) of 7500 msec; 65.7 kHz effective bandwidth; 15 min). T_1 mapping used a variable TR spin-echo approach (TE 8.7 msec; TR 25, 50, 100, 150, 250, 500, 750, 1000, 1500, 2500, 50000, 7500 msec; 119 kHz effective bandwidth; 19 min 19 s). T_1 and T_2 maps acquired were processed using custom scripts in Matlab, with in-line scripts and with the same fitting function for 7 T image sets. The T_1 and T_2 values for individual wells were extracted via histogram analysis of manually drawn regions-of-interest (ROI) using MIPAV software (Bethesda, MD). The longitudinal relaxation time T_1 was quantified using a variable-repetition-time spin-echo pulse sequence (2D-RARE, RARE factor 2; TE 8.7 msec; TR of 25, 50, 100, 150, 250, 500, 750, 1000, 1500, 2500, 5000, 7500 msec; 220 x 160 matrix over 110 × 80 mm field-of-view for 0.5 mm in-plane resolution; 2 mm slice thickness; 119 kHz readout bandwidth; 19 min 19 s acquisition). For each concentration series, T_1_Rel was calculated by linear regression of R_1 ($1/T_1$) and Mn concentration data according to the standard equation:

$$R_1 = R_1^0 + r_1.c(Mn)$$

Where R_1^0 is the relaxation rate of DDIW in the absence of Mn, and c(Mn) is the Mn concentration determined by ICP-OES analysis via iCAP Pro ICP-OES (Thermo Fisher Scientific, Massachusetts, USA) at the Department of Chemistry, University of Toronto.

In vitro H_2O_2 reactivity and oxygen generation capability of TPL-MDNP.

TPL-MDNPs at 100 μM were prepared in 3 mL aliquots for the investigation of their *in vitro* reactivity in the presence of different levels of H_2O_2. Then three concentrations of H_2O_2 were prepared, and 300 μL of samples were added into each of the TPL-MDNPs aliquots to achieve final H_2O_2 concentrations of 500 μM (high concentration), 50 μM (disease concentration), and 5 μM (normal concentration) [62]. The whole spectrum absorbance between the wavelengths of 200–1000 nm of the samples was measured at 0, 1, 2, 5, 10, 20, 30, 45, and 60 min after H_2O_2 addition using UV–vis spectroscopy to observe the color changes of the samples, which directly correlate to the amount of remaining unreacted TPL-MDNPs. Percent of TPL-MDNPs that reacted in the presence of H_2O_2 was calculated based on the UV–vis spectroscopy data at given time points.

To investigate the *in vitro* oxygen generation capability of TPL-MDNPs in the presence of H_2O_2, 130 mL of 100 μM TPL-MDNP was prepared in an Erlenmeyer reaction flask. The reaction flask was then placed in a 37 °C water bath and set up for dissolved oxygen level measurement with edge® Dedicated Dissolved Oxygen Meter (Hanna Instruments, Rhode Island, USA). The sealed system was then purged with N_2 gas until the oxygen level in the TPL-MDNPs suspension reached the baseline level to remove excess oxygen in the system. Following, 0.118 mL of 550 mM H_2O_2 was added to reach a final concentration of 500 μM, and the percent dissolved oxygen level was recorded every 1 min for a total of 90 min or until readings remained stable for 10 min. A similar protocol was used for measurement in the TPL-MDNPs sample without the presence of H_2O_2 for direct comparison of the *in vitro* oxygen generation rates.

4.5. In vitro hemocompatibility analysis of TPL-MDNPs

All animal handling and procedures were conducted strictly following the ethical and legal requirements of the Ontario Animals for Research Act and the Federal Canadian Council on Animal Care guidelines and were approved by the University Animal Care Committee of the University of Toronto and University Health Network. Fresh blood samples were obtained from healthy Sprague Dawley rats via cardiac puncture, and the red blood cells (RBCs) were collected by centrifuging the blood samples at 825×*g* for 5 min. After centrifuging, the level of RBC-containing hematocrit was marked, and the plasma portion was carefully removed and discarded. The RBCs were washed three times by adding saline (pH 7.4) to the marked level. After the wash, the RBCs were resuspended with PBS (pH 7.4), and then the suspension was divided into three tubes. The RBC suspension was treated with the TPL-MDNPs in 5 % dextrose at the final concentrations ranging from 250 μM to 2000 μM of Mn. Negative and positive control samples were added with equal amounts of PBS and 1 % w/v Triton X-100, respectively. The samples were then incubated at 37 °C for 1 h, and then centrifuged at 825×*g* for 10 min. 100 μL supernatant was carefully obtained and transferred to 96-well plates in triplicates. The UV absorbance was then measured at 527 nm on SpectraMax M2 microplate reader (San Jose, California, USA). Percent RBC hemolysis was calculated based on the following formulation, where OD is the optical density of samples:

$$Hemolysis\% = \frac{OD\ (test) - OD\ (negative\ control)}{OD\ (positive\ control)} \times 100\%$$

4.6. Cell lines and cell culture

Human glioblastoma (GBM) U87MG-RED-Fluc (Perkin Elmer, Waltham, MA, USA), TNBC MDA-MB-231-luc-D3H2LN (Caliper Life Sciences (Hopkinton, MA, USA), and prostate PC3 cell lines (ATCC, Virginia, USA) were purchased and grown in Eagle's Minimum Essential Medium (EMEM) (Gibco-Life Technologies, Burlington, ON, Canada), Dulbecco's Modified Eagle Medium (DMEM) (Gibco-Life Technologies), and alpha-modified MEM (α-MEM) (Gibco-Life Technologies) growth medium, respectively, supplemented with 10 % FBS (Invitrogen Inc. Burlington, ON, Canada). Pathogen tests via PCR (Charles River Research Animal Diagnostic Services, Charles River, Massachusetts, USA) were carried out before any *in vivo* studies. For the patient-derived xenografted (PDX)-pancreatic cell line, tumor specimens were collected in serum-free (DMEM) and used within 24 h after culturing. Mouse non-tumorigenic fibroblast NIH3T3 cells were cultured in DMEM supplemented with 10 % FBS. Human non-tumorigenic epithelial cell MCF10A was cultured in DMEM/F12 Medium (Gibco-Life Technologies) supplemented with 5 % horse serum (Gibco-Life Technologies), 20 ng/mL epithelial growth factor (EGF) (Peprotech, Cranbury, New Jersey, USA), 0.5 mg/mL hydrocortisone (Sigma-Aldrich, St. Louis, Missouri, USA), 100 ng/mL cholera toxin (Sigma-Aldrich) and 10 μg/mL insulin (Sigma-Aldrich). All cultures are incubated at 37 °C in a humidified incubator with a 5 % CO_2 atmosphere.

4.7. In vitro cellular uptake

TPL-MDNPs were covalently conjugated to Cyanine5 (Cy5) amine (Lumiprobe, Hunt Valley, Maryland, USA) via NHS/EDC coupling before cell culture treatment to track their cellular uptake in U87MG-luc, MDA-MB-231-luc-D3H2LN, and PC3 cell lines. Cells were seeded at the density of 250,000 cells/plate in 2 mL of growth medium in 35 mm glass-bottom cell culture dishes (MetTek, Ashland, Massachusetts, USA) and incubated overnight at 37 °C, 5 % CO_2 before TPL-MDNPs treatment. Following the addition of Cy5-conjugated TPL-MDNPs at 100 μM Mn, the cultures were incubated for 1h before medium removal and fixation by 1 % paraformaldehyde. Hoechst 33342 was added for nuclei staining 10–15 min before the medium removal and fixation process, and the fixed samples were washed three times with PBS before imaging. Fixed samples were imaged at λ_{ex} = 405 nm (Hoechst 33342) and 638 nm (Cy5-TPL-MDNPs) using TCS SP8 confocal microscope (Concord, ON, Canada) available in the Advanced Optical Microscopy Facility (AOMF) at the Princess Margaret Cancer Research Center (Toronto, ON, Canada).

4.8. In vitro study of MR-contrast enhancement

U87MG-luc cells were seeded in 175 cm^2 tissue culture flasks (Corning, NY, USA) under aerobic and mild hypoxic conditions (1 % O_2) at 37 °C until approximately 80 % flask confluency was reached in all flasks. Following, cells were co-incubated with different treatment media containing 100 μM TPL-MDNP, free Mn^{2+} ions at equivalent concentration, or clinically used gadolinium-based contrast agent, Gadovist®1.0 (gadobutrol, Bayer Inc., Mississauga, ON, Canada) at equivalent concentration for 4 h. 30 min prior to the end of the 4 h post-treatment incubation period, H_2O_2 at 50 μM final concentration was added to one of the culture flask containing TPL-MDNP treatment medium. The treatment medium was then removed from each culture flask and the flasks were thoroughly washed with cold PBS. Cells were then collected and spun down into pellets in 500 μL microfuge tubes at 25×*g* for 5 min. All MR images used a 7 Telsa Biospec system (Bruker Corporation, Ettlingen, DE), equipped with the B-GA12S HP gradient coil insert and running Paravision 360. In vitro experiments utilized an 86 mm inner diameter transmit/receive RF coil, and *in vivo* experiments used the 86 mm inner diameter RF coil for RF transmission and a dedicated receive-only mouse brain coil for MR signal reception. Samples were oriented within a plastic holder and centered within the MR

bore. A series of localizer images were performed to identify a coronal plane, which bisected all tubes at the level of the cell pellets. This plane was prescribed for T1 mapping using a 2D T1-RARE variable repetition-time technique (echo time 7 ms; RARE factor 2; repetition times of 50, 100, 150, 250, 500, 750, 1000, 1500, 2000, 2500, 3500, 5000 ms; 50 × 32 mm field-of-view; 200 × 128 matrix; 0.25 × 0.25 mm in-plane resolution; 1 mm slice thickness; 78.1 kHz bandwidth; 18 min 27 s). T1 maps were generated using Bruker in-line processing and exported in dicom format.

4.9. In vitro cell viability assay

NIH3T3 and MCF10A cell lines were plated at a density of 20,000 cells/well in 200 μL of their corresponding growth media in 96-well plates (R&D systems, Minneapolis, Minnesota, USA). To investigate the *in vitro* viability of the cell lines after treatment with TPL-MDNPs, NPs were added into the wells at final concentrations of 5, 50, 100, 200, and 500 μM Mn, and the plates were incubated at 37 °C, in a 5 % CO_2 incubator for 24 h. 100 μL of 1.2×10^{-3} M MTT in fresh media was used to replace the media in the plates after the incubation period, and the plates were incubated for an additional 4 h. Following, 100 μL of 10 % SDS was added to each well and incubated overnight before measuring the formazan concentrations via absorbance on SpectraMax M2 microplate reader at 540 nm. Percent hemolysis analysis was then carried out based on the absorbance results obtained.

4.10. Orthotopic tumor models

All animal handling and procedures were conducted strictly following the ethical and legal requirements of the Ontario Animals for Research Act and the Federal Canadian Council on Animal Care guidelines and were approved by the University Animal Care Committee of the University of Toronto and University Health Network. All tumor-bearing rodent models and surgical procedures were first optimized before any *in vivo* tumor MRI studies. For the orthotopic brain tumor model, female SCID mice (4–6 weeks old) (OCI, Toronto, Ontario, Canada) were treated with meloxicam at 5 mg/kg of body weight the day before brain tumor implantation for post-surgical pain management. The mice were then anesthetized with 2 % isoflurane/oxygen via inhalation and meloxicam at 5 mg/kg weight before surgery. After skin sterilization, animals were placed in a stereotactic head frame, and a small skin incision was made, followed by a small burr hole in the frontal skull. A 30-gauge needle was used to inject $1.0–5.0 \times 10^4$ human brain glioblastoma U87MG-Luc cells in 2–3 μL of culture medium. After the injection, the skin was closed using sutures and surgical glue as necessary, and daily monitoring of mice for two days following surgery for proper recovery and pain management. Tumor growth was monitored regularly through luciferase expression via *in vivo* bioluminescence imaging before MRI.

For the orthotopic breast tumor model, female SCID mice (4–6 weeks old) (OCI, Toronto, Ontario Canada) were first anesthetized with 2 % isoflurane and shaved over the lateral thorax area, and the skin was sterilized using soap-based iodine/chlorohexidine followed by alcohol-iodine. A 5 mm incision was made in the skin over the lateral thorax after proper sterilization technique, exposing the mammary fat pad. A 40 μL volume of 1.0×10^6 human breast MDA-MB-231-D3H2LN cells in a cell culture medium was injected into the mammary fat pad using a 27-gauge needle. The incision was then closed with sutures and mice were closely monitored for recovery and pain management following the completion of surgery. Mice were monitored daily after tumor cell implantation, and tumor growth was monitored weekly for MRI optimization twice weekly with a caliper for the length (L, largest diameter) and its perpendicular width (W), including skin fold. The volume was calculated using the formula $V = W^2 \times L/2$. MRI was performed when the volume reached approximately 20 mm^2.

For the prostate cancer model, male Sprague Dawley rats (6 weeks old) (Envigo, Indianapolis, Indiana, US) were anesthetized with 2 % isoflurane and injected with meloxicam at 5 mg/kg mice weight before surgery. Rats were chosen over mice for this model for easier and more accurate identification and access to the prostate gland. The lower abdominal region was prepared for surgery and thoroughly disinfected with betadine and alcohol wipe, and then a low midline abdominal incision of approximately 3–4 mm was made. Human prostate PC3 cell suspension was prepared by mixing cell pellets with 10 % Matrigel™ (Product Number 354234, Corning) at 4 °C. The prostate gland was located and 2.0×10^6 PC3 cells in a 20 μL growth medium were injected orthotopically. After the orthotopic cancer cell injection, the incision was closed by suturing with 4.0 absorbable vicryl monofilament sutures for the muscle layer, followed by 4.0 non-absorbable silk sutures for skin using a simple interrupted pattern. Rats were monitored daily after tumor implantation, and tumor growth was monitored weekly via *in vivo* bioluminescence imaging until reaching approximately 50–100 mm^3 (about 3–4 weeks), which is the optimal size and progression for MRI.

For the pancreatic cancer model, the PDX-pancreatic tumor model was established in Dr. David W. Hedley's group following the established protocol [82]. The University Health Network (UHN) Human Research Ethics and Animal Care Committees approved this study protocol (REB# 08–0767 T). Surgical and ascites specimens were collected at the Toronto General Hospital (TGH-UHN) between September 2008 and June 2013 with informed consent from participants. Human research followed the guidelines of the Canada Tri-Council Policy Statement, in accordance with the Declaration of Helsinki. Briefly, cell pellets of patient-derived specimens were mixed with 10 % Matrigel™ in serum-free DMEM at 4 °C and implanted orthotopically in the orthotopic site in Non-Obese Diabetic Severe Combined Immune-Deficient (NOD SCID) mice. Animal care followed the guidelines of UHN Research Institutes' policies and the guidelines of the Canadian Council on Animal Care, and is consistent with ARRIVE guidelines for study design.

All *in vivo* MR imaging used a preclinical small bore 7 T MRI system (Biospec 70/30, Bruker Corporation, Ettlingen, DE), equipped with the BGA-12 gradient coil insert. Mice and rats were anesthetized and maintained at 1.8 % isoflurane throughout experimentation, on the provided slider bed, which included inlaid heated water tubes for thermoregulation using a temperature-controlled pump (Haake P5, Thermo Fisher Scientific, Waltham, MA). Respiration was monitored via a pneumatic pillow taped above the mouse (Model 1030 monitoring and gating system, SA Instruments, Stony Brook, NY). For whole-body pharmaco-kinetic assessment and breast tumor models grown within the lower fat pad, mice were imaged using a 7.2 cm inner diameter quadrature RF coil (Bruker Corporation). Brain tumor mice were imaged using a 7.2 cm inner diameter linearly polarized RF coil for RF transmission, and a dedicated murine brain coil for RF signal reception. Before imaging, 27 G cannulas were placed within the tail veins for contrast agent injection. Imaging then proceeded at baseline and a series of post-injection time points.

4.11. In vivo dose escalation study of TPL-MDNPs

Healthy Sprague Dawley rats (6 weeks old, n = 5 rats per group) were injected with a single dose of 100, 200, 250, and 300 μmol Mn/kg, respectively. The control group for each species was injected with terpolymer solution up to 35 mg per animal. Animals were monitored for changes in their behavior, body weight change, and food consumption up to 5 weeks after the final injection. Multiple-dose toxicity of TPL-MDNPs was also investigated in healthy Sprague Dawley rats (6 weeks old, n = 5 rats per group) at 300 μmol Mn/kg per injection per week for four weeks, with the same monitoring protocol used in single-dose escalation study. For both single- and multiple-dose escalation studies, blood samples of the rats were collected 14 days after injection via tail vein and submitted to the Center of Phenogenomics (Toronto, ON, Canada) for hematology and clinical chemistry analyses. Complete panels of cardiovascular, liver, and renal function were selected for the

clinical chemistry work done on the samples. On day 14 after the last TPL-MDNPs injection time point, animals were euthanized, and major body organs (brain, heart, lungs, liver, spleen, kidneys, and intestine) were collected and prepared for routine hematoxylin and eosin stain. The tissues were examined by a certified histopathologist (HA) for any possible TPL-MDNP accumulation and microscopic changes in the samples.

4.12. In vivo tumor uptake of TPL-MDNPs

Human brain U87-luc and breast MDA-MB-231-luc-D3H2LN tumor-bearing SCID mice were injected with indocyanine green (ICG)-labeled TPL-MDNPs 2 h prior to *in vivo* bioluminescence and fluorescence imaging. After the 2 h post-injection period, bioluminescence signals of luciferase-expressing U87 tumor masses in the animal model were first monitored 15 min post 200 μL D-luciferin injection at 20 mg/mL (Cayman Chemical Company, Ann Arbor, MI, USA). ICG fluorescence signal ($\lambda_{emission}$ = 789 nm, $\lambda_{excitation}$ = 814 nm) in both TPL-MDNPs injected tumor models was then monitored and then compared for signal co-localization in the proximity of tumor masses. Both bioluminescence and fluorescence imaging were carried out using PernElmer Xenogen IVIS Spectrum Imaging System (PerkinElmer, Waltham, MA, USA).

4.13. In vivo pharmacokinetics and tissue clearance studies of TPL-MDNP

Healthy Sprague Dawley rats (6 weeks old, n = 5 rats per group) were injected with a single dose of TPL-MDNPs at 37.5 μmol Mn/kg, and blood samples were collected via tail vein at 0.25, 0.5, 1, 4, and 24 h post-injection time points. Blood samples were then processed for plasma collection, and the resulting plasma samples were analyzed for Mn concentration using ICP-OES. Pharmacokinetic analysis was performed to obtain pharmacokinetic parameters, including area under the curve (AUC), clearance (CL), volume of distribution (V_d), maximum concentration that a drug achieves after dosing (C_{max}), and half-lives ($T_{1/2}$)). The plasma Mn concentration-time profiles were fitted to a 2-compartment model to obtain the micro-rate constants (k_{10}, k_{21}, k_{12}) with the program ADAPT5® (Biomedical Simulation Resource, University of Southern California, Los Angeles, CA, USA).

For the investigation of *in vivo* tissue clearance study via T1W MRI, SCID mice (4–6 weeks old, n = 5 mice per group) were anesthetized by breathing 2 % isoflurane and imaged in a supine position on a custom slider bed. A pneumatic pillow under the thorax/abdomen will provide a signal for both physiologic monitoring and respiratory-gated imaging (SA Instruments, Stony Brook, NY). Before TPL-MDNP injection, animals were prepared via tail vein cannulation with a 27 G needle and a precision line (80 μL internal volume) to enable manual contrast injection at a constant controlled rate. Single injections TPL-MDNPs at 70 μmol Mn/kg were injected into the mice, and the MR T_1-weighted signals were measured using 7 T MRI system fitted with the B-GA12 gradient coil and a 7.2 mm inner diameter quadrature radiofrequency (RF). Whole-body imaging consisted of variable-flip angle T_1 mapping technique at baseline, at 0, 0.5, 1, 2, 4, 24, 48 and 168 h post-injection. Each T_1 mapping acquisition consisted of coronally-oriented respiratory-gated 3D-FLASH image sets at flip angles of 2, 10, 20, and 30° (echo time 3.4 ms; repetition time 30 ms; 280 x 110 x 18 imaging matrix over a 77 × 30.25 × 27 mm field-of-view for 0.275 x 0.275 × 1.5 mm image resolution; 59.4 s per flip angle). The measured signals in major organs (liver, bladder, kidneys, skeletal muscle, and brain) were analyzed, and R_1 was calculated based on T_1 signals measured in these organs during the 168 h post-injection monitoring period.

ICP-OES was also carried out to investigate the amount of Mn in the major organs to confirm the MRI-based clearance results. Healthy Sprague Dawley rats (6 weeks old, n = 5 rats/group) were injected with a single dose of TPL-MDNP at 37.5 μmol/kg Mn of animal weight and were humanely euthanized one week after injection. Rats (6 weeks old, n = 5 rats/group) injected with 0.5 % saline were used as the control group. Major body organs were collected after euthanization, and the weights of the tissue samples were measured and recorded before using nitric acid and H_2O_2 for tissue digestion and release of Mn in the tissues. The digested samples were further processed to remove any solid reminisces, and the aqueous samples were analyzed using ICP-OES to measure the level of Mn.

4.14. Tumoral MRI signal enhancement efficacy and duration studies of TPL-MDNP

Before TPL-MDNP injection, animals were prepared via tail vein cannulation before baseline scanning. Once the baseline scanning was completed, injection with a single dose of TPL-MDNP in all SCID mice models bearing human brain U87MG-luc, breast MDA-MB-231-luc-D3H2LN, or PDX-pancreatic tumors and Sprague Dawley rats bearing human prostate PC3 at 70 μmol/kg Mn of animal weight in mice and 37.5 μmol/kg Mn of animal weight in rats was administered. Following the TPL-MDNP injection, T_1-weighted MR signal maps were generated at 15 min and compared to the MR images generated prior to the TPL-MDNP injection as baselines. In preparation for MRI signal enhancement efficacy in breast and brain tumor-bearing mice models, human breast MDA-MB-231-luc-D3H2LN and brain U87MG-luc xenografted SCID mice (6 weeks old, n = 5 mice/group/model) were injected with single doses of TPL-MDNP at 70 μmol/kg of animal weight. Single doses of Gadovist® 1.0 (gadobutrol, Bayer Inc., Mississauga, ON, Canada) at equivalent dose were also injected into the tumor-bearing mice for comparison of MRI enhancement efficacy comparison. Tumor imaging consisted of transverse anatomic T2-weighted imaging (2D T2w-RARE technique) and serial T_1 mapping (2D variable repetition-time technique, termed variable-TR) at baseline, and on a 15-min cycle to 1 h post-injection. Mice were not moved from the MR scan bed across the imaging series. For breast tumor imaging, the imaging parameters are as follows (T2w-RARE: echo time 54 ms; repetition time 4000 ms; RARE factor 12; 160 x 100 matrix over 32 × 20 mm field-of-view for 0.2 x 0.2 image resolution; at least 32 1-mm slices; 5 averages; 2 min 40 s; variable-TR T_1 mapping: echo time 8.2 ms; 7 repetitions times of 500, 750, 1000, 1500, 2000, 3000, and 5000 ms; 150 x 92 matrix over 33.75 × 20.7 mm field-of-view for 0.225 x 0.225 image resolution; 5 1-mm imaging slices centered on the tumor center; 8 min 1 s). Brain tumor imaging implemented higher resolution revisions to these protocols (T2w-RARE: echo time 72 ms; repetition time 4000 ms; RARE factor 16; 128 x 128 matrix over 16 × 16 mm field-of-view for 0.125 x 0.125 image resolution; at least 7 0.5-mm slices; 5 averages; 2 min 40 s; variable-TR T_1 mapping: echo time 7.7 ms; 8 repetitions times of 250, 500, 750, 1000, 1500, 2000, 2500, and 4000 ms; 128 x 128 matrix over 16 × 16 mm field-of-view for 0.125 x 0.125 image resolution; 5 0.5-mm imaging slices centered on the tumor centrer; 10 min). The T_1-weighted MR signal and R_1 maps were quantified by drawing ROI and measuring SI of the tumor areas. R_1 signals were further analyzed for the two contrast agent groups for signal intensity and duration comparison.

4.15. Statistical data analysis

Power analyses of each *in vitro* and *in vivo* experiment are analyzed using GPower 3.1 software to determine the number of animals needed for statistical significance. OriginPro®8 was used for statistical analysis unless otherwise indicated. For T1W signal analyses of all *in vivo* MRI studies, variable-flip-angle T_1 maps were generated from the individual T_1-weighted images using custom scripts in Matlab (The Mathworks, Natick, MA). Variable-TR T_1 maps were generated using Bruker in-line processing. Image analysis utilized MIPAV software (National Institutes of Health, Bethesda, MD) to calculate mean and standard deviation T_1 values within manually drawn ROI at each time point. All data are presented as means ± standard deviation (S.D.) from three independent trials unless otherwise indicated. Student's t-test was utilized to

determine the statistical significance between two groups. P-values <0.05 were considered statistically significant.

CRediT authorship contribution statement

Tin-Yo C. Yen: Conceptualization, Data curation, Formal analysis, Investigation, Methodology, Writing – original draft, Writing – review & editing, Validation, Visualization. **Azhar Z. Abbasi:** Conceptualization, Data curation, Formal analysis, Methodology, Writing – review & editing, Funding acquisition, Investigation. **Chungsheng He:** Conceptualization, Data curation, Investigation, Methodology, Writing – review & editing, Funding acquisition. **Ho-Yin Lip:** Investigation. **Elliya Park:** Investigation. **Mohammad A. Amini:** Investigation. **Hibret A. Adissu:** Investigation, Writing – review & editing. **Warren Foltz:** Investigation, Writing – review & editing, Formal analysis, Visualization. **Andrew M. Rauth:** Writing – review & editing. **Jeffrey Henderson:** Writing – review & editing. **Xiao Yu Wu:** Conceptualization, Funding acquisition, Writing – review & editing.

Declaration of competing interest

The authors declare that they have no known competing financial interests or personal relationships that could have appeared to influence the work reported in this paper.

Data availability

Data will be made available on request.

Acknowledgement

This work is supported by the CIHR Project Grant (PJT-162301), NSERC Equipment grant (EQPEQ 440689-13), and Killam Research Fellowship from Canada Council for the Arts (702-18-0051) to XYW, Ontario Graduate Scholarship and Departmental Scholarship to TYY and EP, and Mitacs Accelerate Fellowship to MA. Special thanks to **Dr. David W. Hedley's group** for providing the mice with orthotopic PDX pancreatic cancer used in this paper.

Appendix A. Supplementary data

Supplementary data to this article can be found online at https://doi.org/10.1016/j.mtbio.2024.100954.

References

[1] H. Sung, J. Ferlay, R.L. Siegel, M. Laversanne, I. Soerjomataram, A. Jemal, F. Bray, Global cancer statistics 2020: GLOBOCAN estimates of incidence and mortality worldwide for 36 cancers in 185 countries, CA, A Cancer Journal for Clinicians 71 (2021) 209–249, https://doi.org/10.3322/caac.21660.
[2] T. Lancet, Globocan 2018: counting the toll of cancer, Lancet 392 (2018) 985, https://doi.org/10.1016/S0140-6736(18)32252-9.
[3] J.V. Frangioni, New technologies for human cancer imaging, J. Clin. Orthod. 26 (2008) 4012–4021, https://doi.org/10.1200/JCO.2007.14.3065.
[4] M. Alhamami, R.B. Mokhtari, T. Ganesh, J.T. Nofiele, H. Yeger, H.-L.M. Cheng, Manganese-enhanced magnetic resonance imaging for early detection and characterization of breast cancers, Mol. Imag. 13 (2014) 7290, https://doi.org/10.2310/7290.2014.00021, 2014.00021.
[5] W.B. Overcast, K.M. Davis, C.Y. Ho, G.D. Hutchins, M.A. Green, B.D. Graner, M. C. Veronesi, Advanced imaging techniques for neuro-oncologic tumor diagnosis, with an emphasis on PET-MRI imaging of malignant brain tumors, Curr. Oncol. Rep. 23 (2021) 34, https://doi.org/10.1007/s11912-021-01020-2.
[6] M.G. Harisinghani, A. O'Shea, R. Weissleder, Advances in clinical MRI technology, Sci. Transl. Med. 11 (2019), https://doi.org/10.1126/scitranslmed.aba2591 eaba2591.
[7] P.P. Dendy, B. Heaton, Physics for Diagnostic Radiology, third ed., CRC Press, 2011.
[8] M.A. Schmidt, G.S. Payne, Radiotherapy planning using MRI, Phys. Med. Biol. 60 (2015) R323, https://doi.org/10.1088/0031-9155/60/22/R323.
[9] L. Antunovic, R. De Sanctis, L. Cozzi, M. Kirienko, A. Sagona, R. Torrisi, C. Tinterri, A. Santoro, A. Chiti, R. Zelic, M. Sollini, PET/CT radiomics in breast cancer: promising tool for prediction of pathological response to neoadjuvant chemotherapy, Eur. J. Nucl. Med. Mol. Imag. 46 (2019) 1468–1477, https://doi.org/10.1007/s00259-019-04313-8.
[10] M. Beheshti, W. Langsteger, I. Fogelman, Prostate cancer: role of SPECT and PET in imaging bone metastases, Semin. Nucl. Med. 39 (2009) 396–407, https://doi.org/10.1053/j.semnuclmed.2009.05.003.
[11] R. Guo, G. Lu, B. Qin, B. Fei, Ultrasound imaging technologies for breast cancer detection and management: a review, Ultrasound Med. Biol. 44 (2018) 37–70, https://doi.org/10.1016/j.ultrasmedbio.2017.09.012.
[12] H. Chandarana, H. Wang, R.h. n. Tijssen, I.J. Das, Emerging role of MRI in radiation therapy, J. Magn. Reson. Imag. 48 (2018) 1468–1478, https://doi.org/10.1002/jmri.26271.
[13] M. Barkati, S. Van Dyk, F. Foroudi, K. Narayan, The use of magnetic resonance imaging for image-guided brachytherapy, Journal of Medical Imaging and Radiation Oncology 54 (2010) 137–141, https://doi.org/10.1111/j.1754-9485.2010.02152.x.
[14] S. Chin, C.L. Eccles, A. McWilliam, R. Chuter, E. Walker, P. Whitehurst, J. Berresford, M. Van Herk, P.J. Hoskin, A. Choudhury, Magnetic resonance-guided radiation therapy: a review, Journal of Medical Imaging and Radiation Oncology 64 (2020) 163–177, https://doi.org/10.1111/1754-9485.12968.
[15] D.S. Møller, M.I. Holt, M. Alber, M. Tvilum, A.A. Khalil, M.M. Knap, L. Hoffmann, Adaptive radiotherapy for advanced lung cancer ensures target coverage and decreases lung dose, Radiother. Oncol. 121 (2016) 32–38, https://doi.org/10.1016/j.radonc.2016.08.019.
[16] J. Garcia, S.Z. Liu, A.Y. Louie, Biological effects of MRI contrast agents: gadolinium retention, potential mechanisms and a role for phosphorus, Phil. Trans. Math. Phys. Eng. Sci. 375 (2017) 20170180, https://doi.org/10.1098/rsta.2017.0180.
[17] H. Li, Y. Feng, Q. Luo, Z. Li, X. Li, H. Gan, Z. Gu, Q. Gong, K. Luo, Stimuli-activatable nanomedicine meets cancer theranostics, Theranostics 13 (2023) 5386–5417, https://doi.org/10.7150/thno.87854.
[18] X. Xiao, H. Cai, Q. Huang, B. Wang, X. Wang, Q. Luo, Y. Li, H. Zhang, Q. Gong, X. Ma, Z. Gu, K. Luo, Polymeric dual-modal imaging nanoprobe with two-photon aggregation-induced emission for fluorescence imaging and gadolinium-chelation for magnetic resonance imaging, Bioact. Mater. 19 (2023) 538–549, https://doi.org/10.1016/j.bioactmat.2022.04.026.
[19] M. Lauer, A. Lauer, S.-J. You, S. Kluge, E. Hattingen, P.N. Harter, C. Senft, M. Wagner, M. Voss, Neurotoxicity of subarachnoid Gd-based contrast agent accumulation: a potential complication of intraoperative MRI? Neurosurg. Focus 50 (2021) E12, https://doi.org/10.3171/2020.10.FOCUS20402.
[20] J. Ramalho, R.C. Semelka, M. Ramalho, R.H. Nunes, M. AlObaidy, M. Castillo, Gadolinium-based contrast agent accumulation and toxicity: an update, Am. J. Neuroradiol. 37 (2016) 1192–1198, https://doi.org/10.3174/ajnr.A4615.
[21] A. Weller, J.L. Barber, Ø.E. Olsen, Gadolinium and nephrogenic systemic fibrosis: an update, Pediatr. Nephrol. 29 (2014) 1927, https://doi.org/10.1007/s00467-013-2636-z. –1937.
[22] A. Radbruch, L.D. Weberling, P.J. Kieslich, O. Eidel, S. Burth, P. Kickingereder, S. Heiland, W. Wick, H.-P. Schlemmer, M. Bendszus, Gadolinium retention in the dentate nucleus and globus pallidus is dependent on the class of contrast agent, Radiology 275 (2015) 783–791, https://doi.org/10.1148/radiol.2015150337.
[23] H.H. Hu, A. Pokorney, R.B. Towbin, J.H. Miller, Increased signal intensities in the dentate nucleus and globus pallidus on unenhanced T1-weighted images: evidence in children undergoing multiple gadolinium MRI exams, Pediatr. Radiol. 46 (2016) 1590–1598, https://doi.org/10.1007/s00247-016-3646-3.
[24] P. Marckmann, L. Skov, K. Rossen, A. Dupont, M.B. Damholt, J.G. Heaf, H. S. Thomsen, Nephrogenic systemic fibrosis: suspected causative role of gadodiamide used for contrast-enhanced magnetic resonance imaging, J. Am. Soc. Nephrol. 17 (2006) 2359, https://doi.org/10.1681/ASN.2006060601.
[25] T. Grobner, F.C. Prischl, Gadolinium and nephrogenic systemic fibrosis, Kidney Int. 72 (2007) 260–264, https://doi.org/10.1038/sj.ki.5002338.
[26] T. Kanda, K. Ishii, H. Kawaguchi, K. Kitajima, D. Takenaka, High signal intensity in the dentate nucleus and globus pallidus on unenhanced T1-weighted MR images: relationship with increasing cumulative dose of a gadolinium-based contrast, Material, Radiology. 270 (2014) 834–841, https://doi.org/10.1148/radiol.13131669.
[27] Gadovist | Radiology, Radiology Global Master V1. (n.d.). https://www.radiology.bayer.ca/en/gadovist (accessed August 22, 2023).
[28] H.E. Gendelman, V. Anantharam, T. Bronich, S. Ghaisas, H. Jin, A.G. Kanthasamy, X. Liu, J. McMillan, R.L. Mosley, B. Narasimhan, S.K. Mallapragada, Nanoneuromedicines for degenerative, inflammatory, and infectious nervous system diseases, Nanomed. Nanotechnol. Biol. Med. 11 (2015) 751–767, https://doi.org/10.1016/j.nano.2014.12.014.
[29] H. Li, T.J. Meade, Molecular magnetic resonance imaging with Gd(III)-Based contrast agents: challenges and key advances, J. Am. Chem. Soc. 141 (2019) 17025–17041, https://doi.org/10.1021/jacs.9b09149.
[30] C. Chen, J. Ge, Y. Gao, L. Chen, J. Cui, J. Zeng, M. Gao, Ultrasmall superparamagnetic iron oxide nanoparticles: a next generation contrast agent for magnetic resonance imaging, WIREs Nanomedicine and Nanobiotechnology 14 (2022) e1740, https://doi.org/10.1002/wnan.1740.
[31] S. Aime, P. Caravan, Biodistribution of gadolinium-based contrast agents, including gadolinium deposition, J. Magn. Reson. Imag. 30 (2009) 1259–1267, https://doi.org/10.1002/jmri.21969.
[32] D. Pan, A.H. Schmieder, S.A. Wickline, G.M. Lanza, Manganese-based MRI contrast agents: past, present, and future, Tetrahedron 67 (2011) 8431–8444, https://doi.org/10.1016/j.tet.2011.07.076.
[33] D. Stojanov, A. Aracki-Trenkic, D. Benedeto-Stojanov, Gadolinium deposition within the dentate nucleus and globus pallidus after repeated administrations of

gadolinium-based contrast agents—current status, Neuroradiology 58 (2016) 433–441, https://doi.org/10.1007/s00234-016-1658-1.
[34] D. Pan, S.D. Caruthers, A. Senpan, A.H. Schmieder, S.A. Wickline, G.M. Lanza, Revisiting an old friend: manganese-based MRI contrast agents, WIREs Nanomedicine and Nanobiotechnology 3 (2011) 162–173, https://doi.org/10.1002/wnan.116.
[35] M. Alhamami, W. Cheng, Y. Lyu, C. Allen, X. Zhang, H.-L.M. Cheng, Manganese-porphyrin-enhanced MRI for the detection of cancer cells: a quantitative in vitro investigation with multiple clinical subtypes of breast cancer, PLoS One 13 (2018) e0196998, https://doi.org/10.1371/journal.pone.0196998.
[36] H. Sigel, Metal ions in biological systems: volume 37, in: Manganese and its Role in Biological Processes, CRC Press, 2000.
[37] Y.-D. Xiao, R. Paudel, J. Liu, C. Ma, Z.-S. Zhang, S.-K. Zhou, MRI contrast agents: Classification and application (Review), International Journal of Molecular Medicine 38 (2016) 1319–1326, https://doi.org/10.3892/ijmm.2016.2744.
[38] J.L. Aschner, M. Aschner, Nutritional aspects of manganese homeostasis, Mol. Aspect. Med. 26 (2005) 353–362, https://doi.org/10.1016/j.mam.2005.07.003.
[39] A. Takeda, Manganese action in brain function, Brain Res. Rev. 41 (2003) 79–87, https://doi.org/10.1016/S0165-0173(02)00234-5.
[40] T. Grobner, Gadolinium – a specific trigger for the development of nephrogenic fibrosing dermopathy and nephrogenic systemic fibrosis? Nephrol. Dial. Transplant. 21 (2006) 1104–1108, https://doi.org/10.1093/ndt/gfk062.
[41] G. Baio, M. Fabbi, M. Cilli, F. Rosa, S. Boccardo, F. Valdora, S. Salvi, L. Basso, L. Emionite, E. Gianolio, S. Aime, C.E. Neumaier, Manganese-enhanced MRI (MEMRI) in breast and prostate cancers: preliminary results exploring the potential role of calcium receptors, PLoS One 15 (2020) e0224414, https://doi.org/10.1371/journal.pone.0224414.
[42] H. A G, B. R W, K. W, W. T, R. F L W, Magnetic resonance imaging in entomology: a critical review, J. Insect Sci. 3 (2003) 5, https://doi.org/10.1093/jis/3.1.5.
[43] P. Jynge, H. Brurok, A. Asplund, R. Towart, H. Refsum, J.O.G. Karlsson, Cardiovascular safety of MnDPDP and MnCl2, Acta Radiol. 38 (1997) 740–749, https://doi.org/10.1080/02841859709172407.
[44] M.E. Bernardino, J.C. Weinreb, D.G. Mitchell, W.C. Small, M. Morris, Safety and optimum concentration of a manganese chloride–based oral MR contrast agent, J. Magn. Reson. Imag. 4 (1994) 872–876, https://doi.org/10.1002/jmri.1880040620.
[45] J. Greiser, W. Weigand, M. Freesmeyer, Metal-based complexes as pharmaceuticals for molecular imaging of the liver, Pharmaceuticals 12 (2019) 137, https://doi.org/10.3390/ph12030137.
[46] K.A. Davis, B. Lazar, Manganese-based contrast agents as a replacement for gadolinium, Radiol. Technol. 93 (2021) 36–45.
[47] B. Brito, T.W. Price, J. Gallo, M. Bañobre-López, G.J. Stasiuk, Smart magnetic resonance imaging-based theranostics for cancer, Theranostics 11 (2021) 8706–8737, https://doi.org/10.7150/thno.57004.
[48] P. Prasad, C.R. Gordijo, A.Z. Abbasi, A. Maeda, A. Ip, A.M. Rauth, R.S. DaCosta, X. Y. Wu, Multifunctional albumin–MnO2 nanoparticles modulate solid tumor microenvironment by attenuating hypoxia, acidosis, vascular endothelial growth factor and enhance radiation response, ACS Nano 8 (2014) 3202–3212, https://doi.org/10.1021/nn405773r.
[49] C.R. Gordijo, A.Z. Abbasi, M.A. Amini, H.Y. Lip, A. Maeda, P. Cai, P.J. O'Brien, R. S. DaCosta, A.M. Rauth, X.Y. Wu, Design of hybrid MnO2-polymer-lipid nanoparticles with tunable oxygen generation rates and tumor accumulation for cancer treatment, Adv. Funct. Mater. 25 (2015) 1858–1872, https://doi.org/10.1002/adfm.201404511.
[50] A.Z. Abbasi, C.R. Gordijo, M.A. Amini, A. Maeda, A.M. Rauth, R.S. DaCosta, X. Y. Wu, Hybrid manganese dioxide nanoparticles potentiate radiation therapy by modulating tumor hypoxia, Cancer Res. 76 (2016) 6643–6656, https://doi.org/10.1158/0008-5472.CAN-15-3475.
[51] H. Lip, M.A. Amini, A. Zetrini, P. Cai, A.Z. Abbasi, R.G. Bristow, A.M. Rauth, X. Y. Wu, Redox-responsive nanoparticles enhance radiation therapy by altering multifaceted radio-resistance mechanisms in human castration-resistant prostate cancer cells and xenografts, Radiother. Oncol. 170 (2022) 213–223, https://doi.org/10.1016/j.radonc.2022.02.026.
[52] A.E. Zetrini, H. Lip, A.Z. Abbasi, I. Alradwan, T. Ahmed, C. He, J.T. Henderson, A. M. Rauth, X.Y. Wu, Remodeling tumor Immune microenvironment by using polymer-lipid-manganese dioxide nanoparticles with radiation therapy to boost Immune response of castration-resistant prostate cancer, Research 6 (2023) 247, https://doi.org/10.34133/research.0247.
[53] S. Vasseur, F. Guillaumond, LDL Receptor: an open route to feed pancreatic tumor cells, Molecular & Cellular Oncology 3 (2016) e1033586, https://doi.org/10.1080/23723556.2015.1033586.
[54] S. Wagner, A. Zensi, S.L. Wien, S.E. Tschickardt, W. Maier, T. Vogel, F. Worek, C. U. Pietrzik, J. Kreuter, H. von Briesen, Uptake mechanism of ApoE-modified nanoparticles on brain capillary endothelial cells as a blood-brain barrier model, PLoS One 7 (2012) e32568, https://doi.org/10.1371/journal.pone.0032568.
[55] R.X. Zhang, J. Li, T. Zhang, M.A. Amini, C. He, B. Lu, T. Ahmed, H. Lip, A.M. Rauth, X.Y. Wu, Importance of integrating nanotechnology with pharmacology and physiology for innovative drug delivery and therapy – an illustration with firsthand examples, Acta Pharmacol. Sin. 39 (2018) 825–844, https://doi.org/10.1038/aps.2018.33.
[56] J. Kreuter, P. Ramge, V. Petrov, S. Hamm, S.E. Gelperina, B. Engelhardt, R. Alyautdin, H. von Briesen, D.J. Begley, Direct evidence that polysorbate-80-coated poly(butylcyanoacrylate) nanoparticles deliver drugs to the CNS via specific mechanisms requiring prior binding of drug to the nanoparticles, Pharm. Res. (N. Y.) 20 (2003) 409–416, https://doi.org/10.1023/A:1022604120952.
[57] C. He, T. Ahmed, A.Z. Abbasi, L.Y. Li, W.D. Foltz, P. Cai, E. Knock, P.E. Fraser, A. M. Rauth, J.T. Henderson, X.Y. Wu, Multifunctional bioreactive-nanoconstructs for sensitive and accurate MRI of cerebrospinal fluid pathology and intervention of Alzheimer's disease, Nano Today 35 (2020) 100965, https://doi.org/10.1016/j.nantod.2020.100965.
[58] J. Li, P. Cai, A. Shalviri, J.T. Henderson, C. He, W.D. Foltz, P. Prasad, P. M. Brodersen, Y. Chen, R. DaCosta, A.M. Rauth, X.Y. Wu, A multifunctional polymeric nanotheranostic system delivers doxorubicin and imaging agents across the blood–brain barrier targeting brain metastases of breast cancer, ACS Nano 8 (2014) 9925–9940, https://doi.org/10.1021/nn501069c.
[59] U.S.P.C.C. of Revision, The United States Pharmacopeia, 20th Revision: the National Formulary, fifteenth ed., The Convention, 1979.
[60] C. for D.E., Research, Q1A(R2) Stability Testing of New Drug Substances and Products, 2020. https://www.fda.gov/regulatory-information/search-fda-guidance-documents/q1ar2-stability-testing-new-drug-substances-and-products. (Accessed 22 August 2023).
[61] F. Weinberg, N. Ramnath, D. Nagrath, Reactive oxygen species in the tumor microenvironment: an overview, Cancers 11 (2019) 1191, https://doi.org/10.3390/cancers11081191.
[62] N. Yang, W. Xiao, X. Song, W. Wang, X. Dong, Recent advances in tumor microenvironment hydrogen peroxide-responsive materials for cancer photodynamic therapy, Nano-Micro Lett. 12 (2020) 15, https://doi.org/10.1007/s40820-019-0347-0.
[63] T.P. Szatrowski, C.F. Nathan, Production of large amounts of hydrogen peroxide by human tumor Cells1, Cancer Res. 51 (1991) 794–798.
[64] M. Rohrer, H. Bauer, J. Mintorovitch, M. Requardt, H.-J. Weinmann, Comparison of magnetic properties of MRI contrast media solutions at different magnetic field strengths, Invest. Radiol. 40 (2005) 715, https://doi.org/10.1097/01.rli.0000184756.66360.d3.
[65] I.M. Noebauer-Huhmann, P. Szomolanyi, V. Juras, O. Kraff, M.E. Ladd, S. Trattnig, Gadolinium-based magnetic resonance contrast agents at 7 Tesla: in vitro T: 1: relaxivities in human blood plasma, Invest. Radiol. 45 (2010) 554, https://doi.org/10.1097/RLI.0b013e3181ebd4e3.
[66] Berne and Levy Principles of Physiology, Mosby, 2008.
[67] S. Moayyedi, O. Mashinchian, R. Dinarvand, Osmolarity: a hidden factor in Nanotoxicology, DARU J Pharm Sci 24 (2016) 9, https://doi.org/10.1186/s40199-016-0146-9.
[68] M.A. Dobrovolskaia, J.D. Clogston, B.W. Neun, J.B. Hall, A.K. Patri, S.E. McNeil, Method for analysis of nanoparticle hemolytic properties in vitro, Nano Lett. 8 (2008) 2180–2187, https://doi.org/10.1021/nl0805615.
[69] A. Lis, P.N. Paradkar, S. Singleton, H.-C. Kuo, M.D. Garrick, J.A. Roth, Hypoxia induces changes in expression of isoforms of the divalent metal transporter (DMT1) in rat pheochromocytoma (PC12) cells, Biochem. Pharmacol. 69 (2005) 1647–1655, https://doi.org/10.1016/j.bcp.2005.03.023.
[70] J. Hu, Toward unzipping the ZIP metal transporters: structure, evolution, and implications on drug discovery against cancer, FEBS J. 288 (2021) 5805–5825, https://doi.org/10.1111/febs.15658.
[71] A.S. Wadajkar, J.G. Dancy, D.S. Hersh, P. Anastasiadis, N.L. Tran, G.F. Woodworth, J.A. Winkles, A.J. Kim, Tumor-targeted nanotherapeutics: overcoming treatment barriers for glioblastoma, WIREs Nanomedicine and Nanobiotechnology 9 (2017) e1439, https://doi.org/10.1002/wnan.1439.
[72] K. Greish, Enhanced permeability and retention (EPR) effect for anticancer nanomedicine drug targeting, in: S.R. Grobmyer, B.M. Moudgil (Eds.), Cancer Nanotechnology: Methods and Protocols, Humana Press, Totowa, NJ, 2010, pp. 25–37, https://doi.org/10.1007/978-1-60761-609-2_3.
[73] D. Kalyane, N. Raval, R. Maheshwari, V. Tambe, K. Kalia, R.K. Tekade, Employment of enhanced permeability and retention effect (EPR): nanoparticle-based precision tools for targeting of therapeutic and diagnostic agent in cancer, Mater. Sci. Eng. C 98 (2019) 1252–1276, https://doi.org/10.1016/j.msec.2019.01.066.
[74] T.J. Clough, L. Jiang, K.-L. Wong, N.J. Long, Ligand design strategies to increase stability of gadolinium-based magnetic resonance imaging contrast agents, Nat. Commun. 10 (2019) 1420, https://doi.org/10.1038/s41467-019-09342-3.
[75] M. Rogosnitzky, S. Branch, Gadolinium-based contrast agent toxicity: a review of known and proposed mechanisms, Biometals 29 (2016) 365–376, https://doi.org/10.1007/s10534-016-9931-7.
[76] B. Tamrazi, C.-S.J. Liu, S.Y. Cen, M.B. Nelson, G. Dhall, M.D. Nelson, Brain irradiation and gadobutrol administration in pediatric patients with brain tumors: effect on MRI brain signal intensity, Radiology 289 (2018) 188–194, https://doi.org/10.1148/radiol.2018173057.
[77] A.B. Nair, S. Jacob, A simple practice guide for dose conversion between animals and human, J. Basic Clin. Pharm. 7 (2016) 27–31, https://doi.org/10.4103/0976-0105.177703.
[78] R.X. Zhang, P. Cai, T. Zhang, K. Chen, J. Li, J. Cheng, K.S. Pang, H.A. Adissu, A. M. Rauth, X.Y. Wu, Polymer–lipid hybrid nanoparticles synchronize pharmacokinetics of co-encapsulated doxorubicin–mitomycin C and enable their spatiotemporal co-delivery and local bioavailability in breast tumor, Nanomed. Nanotechnol. Biol. Med. 12 (2016) 1279–1290, https://doi.org/10.1016/j.nano.2015.12.383.
[79] R.N. Kularatne, R.M. Crist, S.T. Stern, The future of tissue-targeted lipid nanoparticle-mediated nucleic acid delivery, Pharmaceuticals 15 (2022) 897, https://doi.org/10.3390/ph15070897.

[80] A. Shalviri, W.D. Foltz, P. Cai, A.M. Rauth, X.Y. Wu, Multifunctional terpolymeric MRI contrast agent with superior signal enhancement in blood and tumor, J. Contr. Release 167 (2013) 11–20, https://doi.org/10.1016/j.jconrel.2013.01.014.

[81] S. Nagayama, K. Ogawara, Y. Fukuoka, K. Higaki, T. Kimura, Time-dependent changes in opsonin amount associated on nanoparticles alter their hepatic uptake characteristics, Int. J. Pharm. 342 (2007) 215–221, https://doi.org/10.1016/j.ijpharm.2007.04.036.

[82] N.-A. Pham, N. Radulovich, E. Ibrahimov, S.N. Martins-Filho, Q. Li, M. Pintilie, J. Weiss, V. Raghavan, M. Cabanero, R.E. Denroche, J.M. Wilson, C. Metran-Nascente, A. Borgida, S. Hutchinson, A. Dodd, M. Begora, D. Chadwick, S. Serra, J. J. Knox, S. Gallinger, D.W. Hedley, L. Muthuswamy, M.-S. Tsao, Patient-derived tumor xenograft and organoid models established from resected pancreatic, duodenal and biliary cancers, Sci. Rep. 11 (2021) 10619, https://doi.org/10.1038/s41598-021-90049-1.